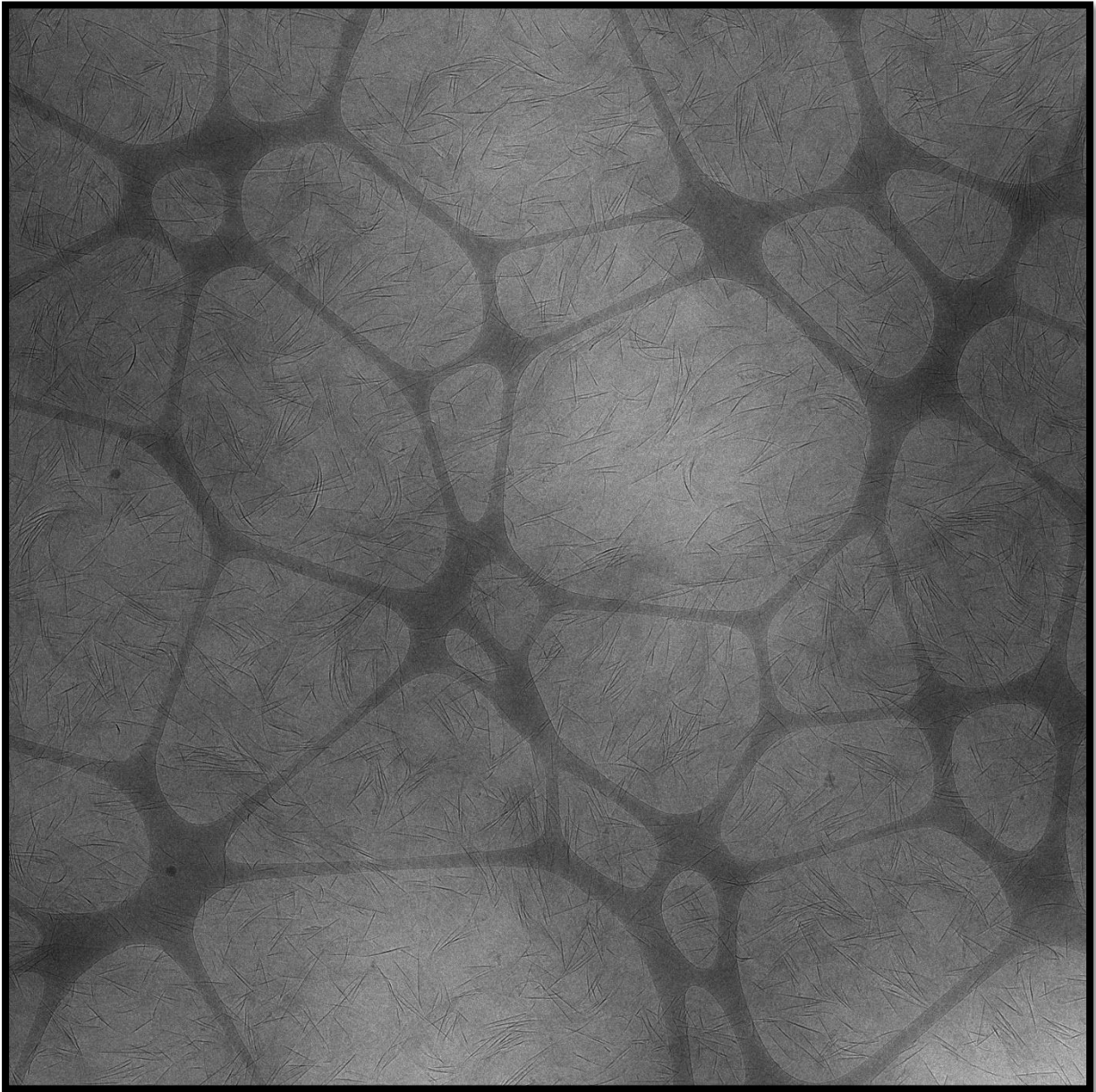


Aqueous self-assembly behaviour alteration derived  
from primary structure changes of model peptides



Marcus Bäcklund

Faculty of Science, Lund university

Department of Chemistry

# Abstract

Understanding of the self-assembly behaviour of peptides is of great interest within several different areas such as neurodegenerative diseases, biotechnology, and peptide pharmaceuticals. In this work we have compared the impact on the self-assembly behaviour derived from systematic changes of the primary structure of A8K, where A denotes alanine and K lysine. Model peptides derived from A8K included in this work are KA8, G8K, and A4KA4, where G denotes glycine. In addition, we have also studied the self-assembly behaviour of binary mixtures of the model peptides to probe coaggregation of the different model peptides. To determine the aggregate structure small and wide-angle x-ray scattering and cryo TEM experiment were performed. Furthermore, to determine the secondary structure, we performed measurements using circular dichroism and infrared spectroscopy. We also probed the solubility of the model peptides through static light scattering experiments.

From our results we can derive, that replacing alanine with the less hydrophobic amino acid glycine leads to a higher critical aggregation concentration, as expected. Furthermore, the change removes much of the chirality of the model peptide, leaving lysine as the only chiral amino acid in the peptide. The result from this is that G8K form two-dimensional disc-like aggregates, whereas A8K aggregates into twisted one-dimensional fibres.

A higher peptide solubility is also observed for A4KA4 where the lysine amino acid has been placed in the middle of the peptide, presumably due to a destabilization of the laminated beta-sheet structure as the bulky lysine sidechain is accommodated within the peptide aggregates. By reversing the amino acids sequence, we observe a minor structural change for KA8. For the binary mixtures of A8K or KA8 and G8K, we can conclude that they coaggregate with aggregate properties reminiscent of the alanine model peptide.

# Populärvetenskaplig sammanfattning

Peptider är mindre versioner av protein. Det som man vanligtvis kan läsa på innehållsförteckningen på de flesta matvaror i dagen samhälle. Peptiderna i sig består av aminosyror som kan anses vara de minsta byggstenarna för peptider och proteiner.

Peptider och proteiner spelar en stor roll i våra biologiska system. Proteiner och peptider bidrar till flera viktiga processer. Proteiner hjälper till med att få vårt blod att koagulera när vi skadar oss. De kan hjälpa till med matsmältningen och mycket annat i kroppen.

Många processer i kroppen behöver ha peptider eller proteiner för att saker ska gå rätt till. Men det är inte alltid saker går som det ska. En alltför vanlig sjukdom vi har idag är Alzheimers.

Alzheimer och många andra sjukdomar kan kopplas till proteiner och peptider där något går fel. För Alzheimers så börjar proteiner klumpa ihop sig för att något har gått fel vid tillverkningen av proteinerna.

Därför så finns det ett stort intresse av att förstå vilka faktorer som bidrar till hur peptider klumpar ihop sig. Därför så studerar detta arbete en serie av fyra konstgjorda modellpeptider. Varje peptid är framställd men en ändring sinsemellan. Detta för att kunna urskilja hur en liten ändring av modellpeptiden kan bidra till förändrat beteende i ett större perspektiv.

# Table of contents

<b>1.</b>	Introduction.....	5
<b>2.</b>	Material and methods.....	7
2.1	Sample preparation.....	7
2.2	Circular dichroism.....	7
2.3	Small angle X-ray scattering.....	8
2.4	ATR-FIR.....	9
2.5	Static light scattering.....	11
2.6	Cryo TEM.....	11
<b>3.</b>	Results and discussion.....	12
3.1	Aqueous self-assembly of G8K.....	12
3.2	Comparing the self-assembly behaviour of KA8, A4KA4, and KA8.....	19
3.3	Binary mixtures of model peptides.....	28
3.3.1	Binary mixture of A6K and A10K.....	28
3.3.2	Binary mixture of A8K and KA8.....	29
3.3.3	Binary mixture of A8K and G8K.....	30
3.3.4	Binary mixture of KA8 and G8K.....	32
<b>4.</b>	Conclusions.....	35
<b>5.</b>	Outlook.....	36
<b>6.</b>	Acknowledgements.....	37
<b>7.</b>	References.....	38
<b>8.</b>	Appendix.....	41

# 1. Introduction

Amino acids are the building block of any peptide or protein. Amino acids come in many different forms, characterized by their side chain. Each amino acid has an alpha-carbon, the alpha carbon is the central atom in the amino acid. The alpha carbon is connected to an amino acid specific sidechain, an amine, and a carboxylic acid. Generally, 50 or less amino acids and the molecule is referred to as a peptide. If you have more than 50 amino acids, you have a protein instead.

Understanding peptide aggregation behaviour on a fundamental level is of interest in several different fields such as neurodegenerating diseases, biotechnology, and peptide pharmaceuticals.

A hallmark for neurodegenerating diseases, such as Alzheimer's, is the aggregation of amyloid polypeptide fibrils (M. Dobson, 1999). Understanding the aggregation process is key for developing future therapeutics. Furthermore, understanding co-aggregation effects are of interest as well, as the presence of one polypeptide might catalyse the aggregation of other less aggregation prone polypeptides. (Cukalevski et al., 2015)

Furthermore, peptides are also used in bio nanotechnology, as building blocks for more complex materials used in synthesis and fabrication of devices. Whilst proteins are used for more complex tasks, peptides can aggregate into supramolecular structures prone to undergo changes when the physiochemical environment is changed. Thus, conformation changes of peptide materials induced by external stimuli can be utilized as sensors and as responsive smart materials. (De La Rica & Matsui, 2010)

Peptides are of great interest for the pharmaceutical market, being midway between small molecules and more complex biopharmaceuticals. Peptide therapeutics have shown great promise and with further untapped potential for future therapeutics. However, challenges such as aggregation and solubility of the peptide pharmaceuticals must be overcome. Thus, for natural peptides there is a need to address these issues. Methods to approaching these problems include destabilization of hydrophobic patches of the peptides and methylation. Given the pH of the intended final product, charge distribution and isoelectric points also of importance. (Fosgerau & Hoffmann, 2015)

The sequence of amino acids is referred to as the primary structure of a peptide or protein. It begins at the amino-terminal (N) and ends at the carboxyl terminal (C). The secondary structure holds information about repeating local structures, stabilized by hydrogen bonds. Amongst secondary structures we may find alpha helices and beta-sheets. Furthermore, there is tertiary and quaternary structures who describe entire proteins.

Aggregation of peptides is complex interchange between several different factors. Of main interest is the hydrophobic interaction with water and hydrogen bonds between peptides stabilising secondary structures. What kind alteration of the primary structure of a model peptide could impact its self-assembly behaviour? Could it be possible to derive a change in secondary structure from a specific change in the primary structure of a model peptide?

This aim of this work is to analyse possible changes induced in the secondary structure of aggregated model peptides as the primary structure of the model peptides are altered. Ideally, it would be possible to map one change in the primary structure to one change in the secondary structure.

Three peptides will be of interest within this work, alanine, glycine, and lysine. Alanine and glycine have similar sidechains, a hydrogen for glycine and a methyl group for alanine. The sidechain of lysine is longer with four carbons and an amine at the end. Alanine, glycine, and lysine is shown figure 1.

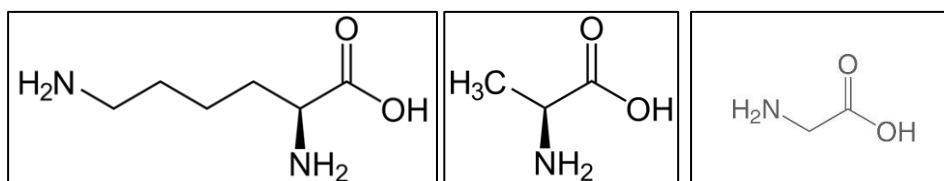


Figure 1. Lysine(left), alanine(middle) and glycine(left).

These peptides will compose four different model peptides as the base for thesis. We have three alanine model peptides where we alter the position of lysine within the primary structure of the model peptide. They will be addressed as A8K, KA8 and A4KA4. Thus, the lysine will be put at the N-terminus, C-terminus, and in the middle of the primary structure. Furthermore, in the fourth case the alanine will be switched for glycine resulting in the peptide G8K. Model peptides are shown in figure 2.

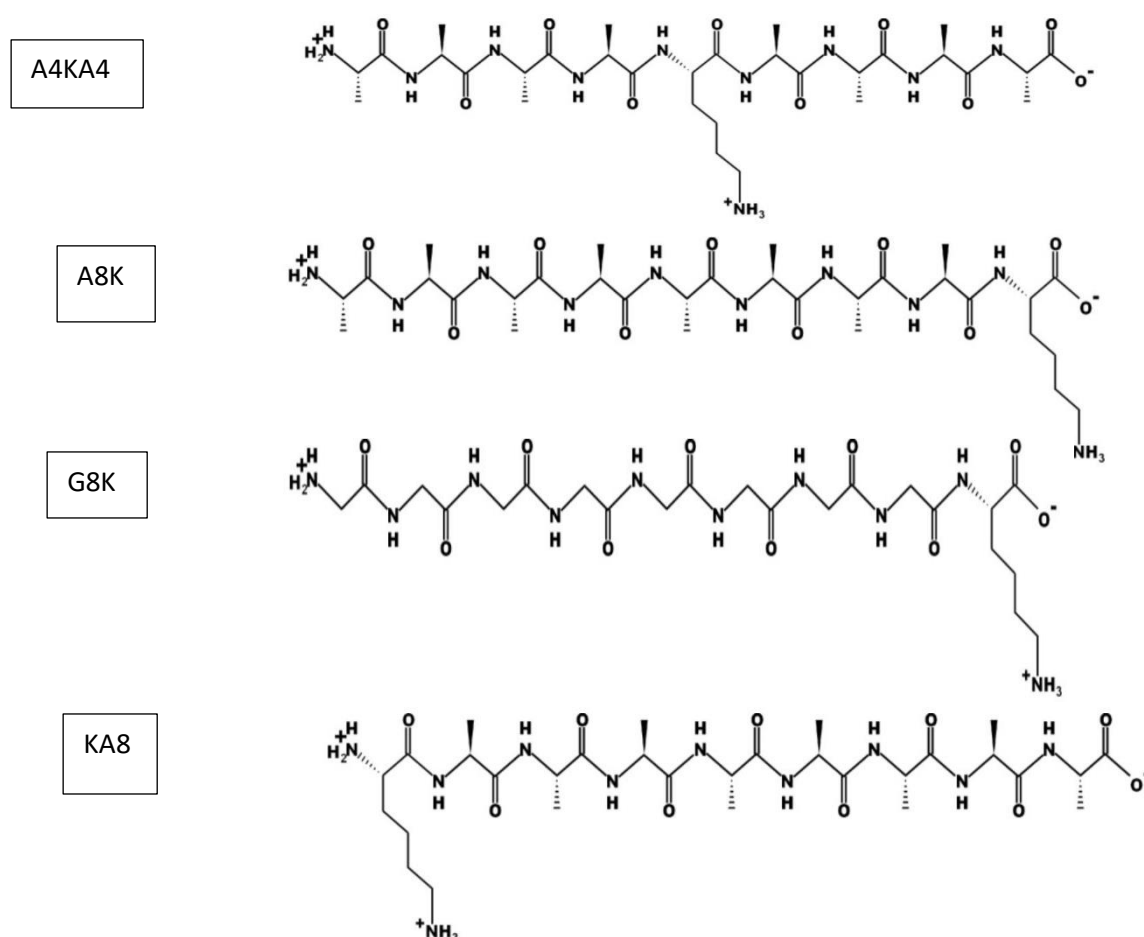


Figure 2. Model peptides A4KA4, A8K, G8K and KA8

Previous work in the field of peptides self-assembly systems have been made by (Zhang, 2003; Zhao et al., 2008). Research on the colloidal and molecular aspects of the  $A_nK$  model peptide system have lately been made by (Cenker et al., 2014; Rüter, 2020).

The model peptide primary structures within this work are derived from the previous work by (Rüter, 2020). Complementary projects have evolved to include binary mixtures of the previously mentioned model peptides and  $A_nK$  peptides of different length.

Previous work by (Rüter, 2020) have extensively described the molecular and colloidal aspects for  $A_{10}K$  and  $A_8K$ . Therefore, the length of the model peptide is of interest as well. Justifying a side project regarding suggested coaggregation behaviours of model peptides of different lengths.

This work entails the exploratory work of the author. Focusing on explaining what behaviour that can be observed for the new model peptides. And when data supports it, explain why we can observe a certain behaviour.

## 2. Materials and methods

### 2.1 Sample preparation and materials.

Peptides samples were received from CPC scientific Inc with a peptide purity at around 95% and with trifluoroacetic acid (TFA) as the counterion. Vials and NMR tubes were thoroughly washed with soap and de-ionized water several times then blow dried with air. NMR tubes had an additional wash with a 2% Hellmanex solution.

Sample preparation used filtered, 0.2 $\mu$ m GHP membrane, Milli-Q water. The peptides were measured on high accuracy scales. Samples were prepared by weighing peptide and water into glass vials.

### 2.2 Circular dichroism (CD)

CD measurements were made with a Spectropolarimeter of the manufacturer Jasco, model J-715. The samples were applied to either a 0.1mm or a 0.01 mm cell, to get measurable data and to avoid over absorption at the detector due to samples having a too high absorption depending on the sample concentration. Backgrounds measurements, of Milli-Q water were performed between samples measurements and the cells were washed with a 2% Hellmanex solution between measurements. Measurements, of purified water, between samples were done to assure that the cells were cleaned of leftover residues, peptide monomers, as they would contribute to the spectra of sample measurements.

In CD one measures the difference in absorption of right, respectively left, polarized light of a sample. Initially the radiated light, left and right polarized, have the same magnitude. However, when the radiated light is absorbed it can do so in several ways. No difference in absorbed light would mean that detected light, of different polarizations, would be of the same magnitude. Thus, not leading to any observable CD spectra.

For light to be absorb, there needs to be an optically active component. For the case of polypeptides, the optically active component is the amino acids. This is the case for all amino

acids except one amino acid. Glycine is the only amino acid not optically active since its  $\alpha$ -carbon is bonded to two hydrogen.

Different protein secondary structures will induce characteristic internal conformations of the peptide bonds of the polypeptide/protein. Different internal conformation will leads to specific absorption patterns for different kinds of secondary structures, as seen in figure 3. (Kelly et al., 2005)

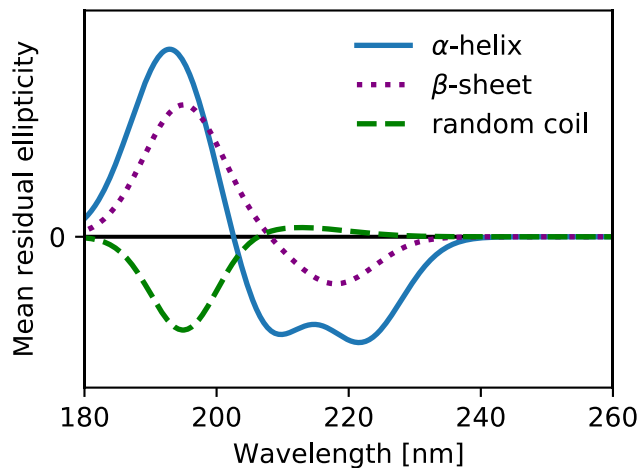


Figure 3. CD fingerprint spectra for protein secondary structures.

## 2.3 Small and wide-angle x-ray scattering (SAXS/WAXS)

Small angle x-ray scattering measurements were performed on a Ganesha 300XL (Saxslab). By using a moveable detector, a wide  $q$ -range can be measured. Thus, a WAXS stage was used to include both small and wide-angle measurements. Measurements were made at room temperature.

Initial data treatment was made by SaxsLab Graphical user Interface(GUI), transforming the two-dimensional data to a one-dimensional data by radially averaging the intensity. Furthermore, additional analysis was made by fitting scattering models to the measured data using SasView([www.sasview.com](http://www.sasview.com)).

Small angle x-ray scattering is commonly used for characterization of soft matter systems. The method radiates the sample with x-rays and the molecules in the sample will interact with the incoming radiation and scatter it in a way depicting the properties of the given sample.

When a sample is radiated with the primary beam scattering will occur. The scattered intensity from the sample will deviate from the primary beam, the angle of deviation is called the scattering angle, denoted  $\theta$ . As the x-rays are scattered by the particles in the sample, a wave of radiation will arise from the position of the molecules. This wave will then create interference patterns at the detector where the intensity of the scattering pattern is dependent on the scattering angle. This creates a distinctive two-dimensional pattern at the detector. This two-

dimensional pattern will carry information about the internal structure of the molecule, orientation, and distances of atoms within the molecule.

To have a uniform way to present data, scattering intensity is often plotted against a scattering vector  $q$ , see Eq 1, where  $\lambda$  is the wavelength of the primary beam and  $\theta$  is the scattering angle. The unit for the scattering vector is inverse length usually in  $\text{nm}^{-1}$  or  $\text{\AA}^{-1}$ .

$$q = \frac{4\pi}{\lambda} * \sin(\theta/2) \quad (1)$$

When representing scattering data, we often do so in a reciprocal manner due to the scattering vector having the inverse relationship to a real length scale. At lower  $q$ -values we obtain information over longer length scales of the sample, and at higher  $q$  values smaller length scales. Furthermore, the value of the scattering angle, and thus the scattering vector, is dependent on the distance from the sample to the detector. To measure at a range of  $q$  values the distance between the sample and the detector is altered. The distance from the detector to the sample leads to two different methods of measuring scattering. SAXS scattering corresponds to longer distances between the sample and the detector, and therefore lower  $q$ -values. WAXS has shorter distances from the sample to the detector, resulting in higher  $q$ -values.

The scattered intensity of a sample can be described by Eq 2. Where  $\Phi_p$  is the volume fraction of the sample,  $\Delta\rho^2$  is the difference in scattering length density (SLD) between the sample and the solvent squared,  $V_p$  is the particle volume,  $P(q)$  is the form factor and  $S(q)$  is the structure factor.

$$I(q) = \Phi_p \Delta\rho^2 V_p P(q) S(q) \quad (2)$$

The difference in SLD is derives a difference in contrast for the solvent and sample. With no contrast between the sample and the solvent, no scattering pattern can be expected. The form factor,  $P(q)$ , holds information about intramolecular scattering while the structure factor,  $S(q)$ , holds information about intermolecular scattering.

## 2.4 Attenuated total reflectance Fourier transformed Infrared spectroscopy (ATR-FTIR)

FTIR is a reliable method that procures information about the composition of the sample and furthermore its structure. FTIR is adequate to probe properties of biological samples such as protein structures and to highlight secondary structures of peptide aggregates. The method radiates the sample with an infrared beam that is absorbed by different bonds in the sample and their vibrational energies. Different bonds will absorb at different frequencies corresponding to the energy needed to perturb the specific bond.

A difference between transmission FTIR and ATR is the preparations needed and the accuracy of the measurements. ATR requires less preparation and is a bit less precise.

Experiments were performed on a Nicolet 6700 FTIR instrument with an ATR attachment. Samples were applied to the diamond crystal and measurements were performed. In the case of the measurements of dried samples, the measurement was performed when the auto-collecting

mode of the instrument showed no change in the spectrum as the sample was drying. Measurements on dried samples were made to improve sample signal for lower concentration ranges. Initial background subtraction was made on the Thermo Omnic software.

In figure 4 as ATR experimental setup is shown. The incoming infrared beam is reflected on the surface where the sample is placed. At the interface, an evanescent wave protrudes into the sample leading to an attenuation of the wave dependent on the absorption properties of the sample. The wave then returns into the crystal and eventually reaches the detector. Dependent on the experimental setup the incoming infrared beam might probe the sample several times or once.

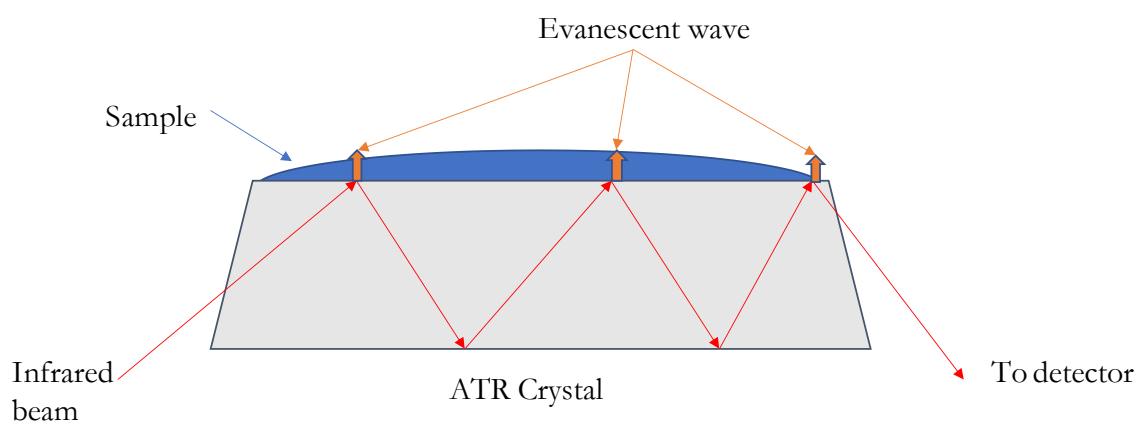


Figure 4. Basic principle for ATR-FTIR measurements.

When infrared light is absorbed by a molecule it will excite a vibrational transition of certain bonds within the given molecule, to a quantized amount of energy. It is an interaction between the dipole moment of a molecule and the incoming electromagnetic waves. For far- and mid-infrared frequencies ( $14000 - 30 \text{ cm}^{-1}$ ) their oscillating electrical fields of the electromagnetic waves will have the same frequency as the vibrations of dipolar bonds of molecules. Thus, the absorption of infrared light correlates to that of dipolar bond vibrating with the same frequency as that of the oscillating electrical field of the absorbed infrared radiation.

Furthermore, the infrared absorption bands, of dipolar bonds within a molecule are affected by several factors. An absorbance band is a frequency area where a specific bond is absorbing radiation. For this work we have focused on the intermolecular interactions of peptides. As the nature of inter- and intramolecular interactions will impact the absorbance bands of a given dipolar bond. Differences in secondary structure would therefore be detectable.

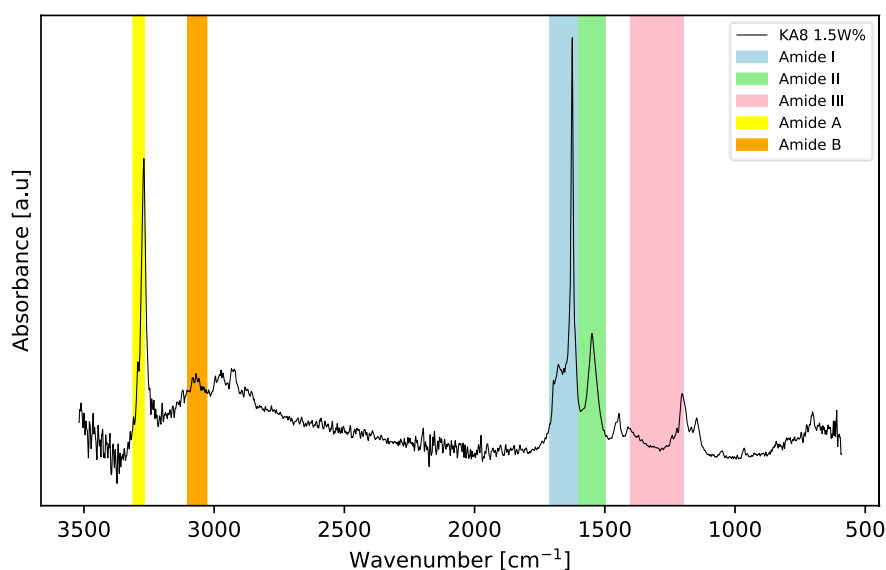


Figure 5. Amide regions of interest for peptide analysis shown together with a KA8 sample.

The backbone of a peptide is composed of linked amino groups linked together by amides. Different parts of the amide group will have an absorbance band at different frequencies, as they are taking part in different kind of bonds. The absorbance at certain frequencies correlates with vibrational transitions for a specific part of the amide group. A specific secondary structure of an aggregated peptide would then lead to absorbance in a specific band, being dependent on intra- and intermolecular environment and character of hydrogen bonds of the aggregate.

The amide A region correlates to an N-H stretching and the position is dependent on the strength of the hydrogen bond. It is exclusive for the NH group of the peptide backbone.

The amide region of most importance is the amide I region, with a major contribution from a secondary structure affected C=O bond. The only sidechain contribution of interest in this work is that of the lysine side chain with absorbance at around  $1630\text{ cm}^{-1}$  (Barth, 2000). It should also be noted that the counterion from the solid-state synthesis, TFA, absorbs around  $1673\text{ cm}^{-1}$  (Haris & Chapman, 1995). The amide I region is the most sensible region when it comes to secondary structure determination as certain secondary structures have a characteristic band absorbance in the amide I region, see table M1

Table M1

Band assignment for amide region I for different secondary structures, extreme values in parenthesis.

Secondary structure	Band positions ( $\text{H}_2\text{O} / \text{cm}^{-1}$ )
$\alpha$ - helix	1654 (1648-1657)
$\beta$ - sheet	1633 (1623-1641) 1684 (1674-1695)
Turns	1672 (1662-1686)
Disordered	1654 (1642-1657)

The amide II region is a combination of NH, CO, CC, and NC vibrations. Contributions from side chains are negligible and the relation between secondary structure and absorbance bands

lack a clear correlation. Amide region III is furthermore a complex sum of contributions from different vibrations and is not adequate for second structure analysis.

(Barth, 2007; Barth & Zscherp, 2002)

## 2.5 Static light scattering (SLS)

Samples were measurements were performed on a Goniometer ALV DLS/SLS(ALV-Laser). Samples were measured in NMR-tubes at a 90° angle and the average value of three measurements for the ratio of scattered versus incoming intensity were used for data analysis. Measurements that deviated in scattered intensity were redone.

Static light scattering theory is shared with that of any scattering method. The approach for static light scattering in this thesis is to determine the critical aggregation concentration (CAC) of the model peptides. As the monomers in solution will start to aggregate, we can expect the aggregates to start scatter light as larger particles are formed.

## 2.6 Cryo Transmission electron spectroscopy (TEM)

Samples were quickly diluted for each respective peptide. The samples were then applied to an electron microscope grid and blotted to a thin layer. Immediately after a successful blotting the sample is plunged into nitrogen, snap-freezing the water and the sample. The time from dilution to the samples being frozen in liquid nitrogen was 2 minutes or less. The blotting and the dilution were done to ensure that the amount of sample would be appropriate when observed in the electron microscope. As to much sample would lead to cluttered images. The snap-freezing is important as the water is kept from crystalizing as it freezes. Crystalline ice would compromise the images if the water were not frozen fast enough.

Transmission electron microscopy is an imaging technique relying on the same principle as the microscope using light, only that electrons are used instead of light. (Carroni & Saibil, 2016)

# 3. Results & Discussion

## 3.1 Aqueous self-assembly of G8K

This chapter entails the observed self-assembly behaviour of the G8K model peptide. The main objective for studying G8K was to characterize the effects on the self-assembly behaviour by altering the hydrophobicity of the model peptide, in comparison with A8K. Thus, alanine was exchanged for glycine. The change in hydrophobicity is derived from the change in sidechains for the amino acids. The sidechain for alanine is a methyl group and for glycine a hydrogen. Furthermore, moving from alanine to glycine caused another important change as glycine is achiral. The alpha carbon is bonded to two hydrogen instead of a hydrogen and a methyl group.

At first the solubility of G8K was of interest. Thus, the CAC was determined by performing light scattering experiments. Figure 6 shows the scattered intensity as a function of concentration the peptide. As aggregates form more light will be scattered. The amount of scattered light should increase with the amount of aggregates formed. As shown in figure 6, the critical aggregation

concentration can be estimated to be  $3 \pm 0.5$  wt.%. Compared to A8K that aggregates at much lower concentrations, at around 0.1wt%(Cenker et al., 2014). This is not unexpected as the hydrophobicity changes greatly when exchanging a hydrophobic methyl group for a hydrogen.

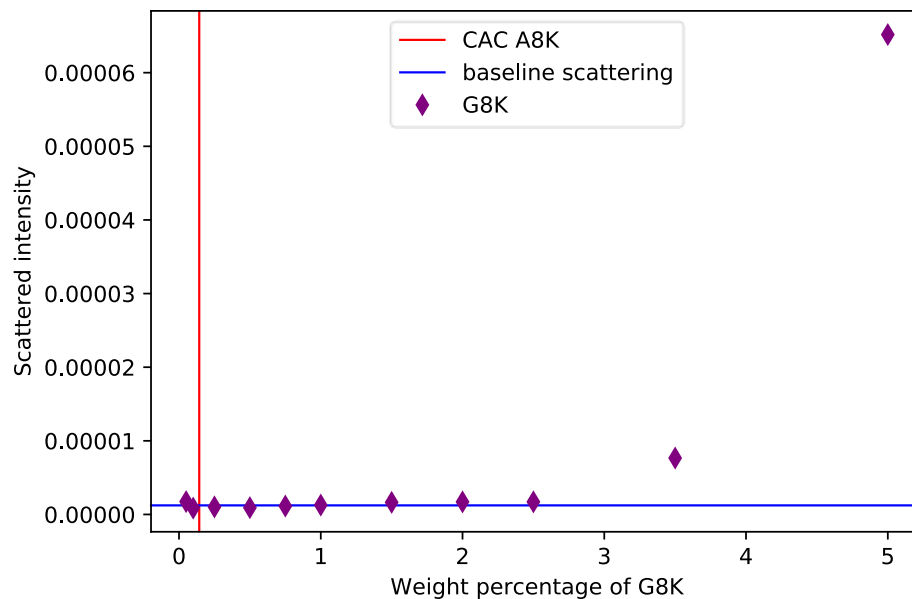


Figure 6. The scattered intensity of G8K as a function of wt%. The baseline scattering is the average value from the point of low scattered intensity. As it is scattering from monomers the scattering should slightly increase as the monomer concentration rises.

G8K has proven to be an interesting model peptide. Previously we have seen the peptides, AnK form fibrils (Cenker et al., 2014; Rüter et al., 2019). Furthermore, SAXS measurements were performed to study the inter and intramolecular properties of the aggregated monomers. Initial SAXS measurement suggests that G8K form aggregates that form two-dimensional shapes. The initial slope of -2.2, derived from the values in the low  $q$ -range, in figure 7 indicates the presence of two-dimensional shape(Schnablegger & Singh, 2011). To further characterize the scattering patterns from the G8K peptides a thin disc model in combination with a monomeric Gaussian polymer coil model was chosen to simulate the scattering data. Since G8K have high solubility the contribution from the monomers is not negligible, as we expect that a considerable part of the sample will not have aggregated due to the sample concentration only being 2 wt% above the CAC.

Furthermore, a specific diffraction pattern has in previous studies been present in the WAXS region of the measurements of the alanine model peptides. Due to the local packing of the model peptides diffraction patterns will arise due the crystalline packing(Kuczera et al., 2020). This is notably not present for G8K. However, if the sample is left to age a small peak can be observed at  $q = 1.4 \text{ \AA}^{-1}$ . This corresponds to  $4.5 \text{ \AA}$  and is found in other systems as corresponding to the beta strand distance within beta-sheets.

In figure 7 we show three different models. The black dashed model for both sample measurements (2 days and 66 days) assumes a single disc with a thickness of 3 nm, about the length of a G8K peptide. However, the blue dashed model stacks discs instead of a single disc. This leads to a noticeable better fit for the early measurement. The same parameter, stacking

discs, does not fit at all for the later measurement. The radius of gyration for the polymer coil is set to 7 Å for all models.

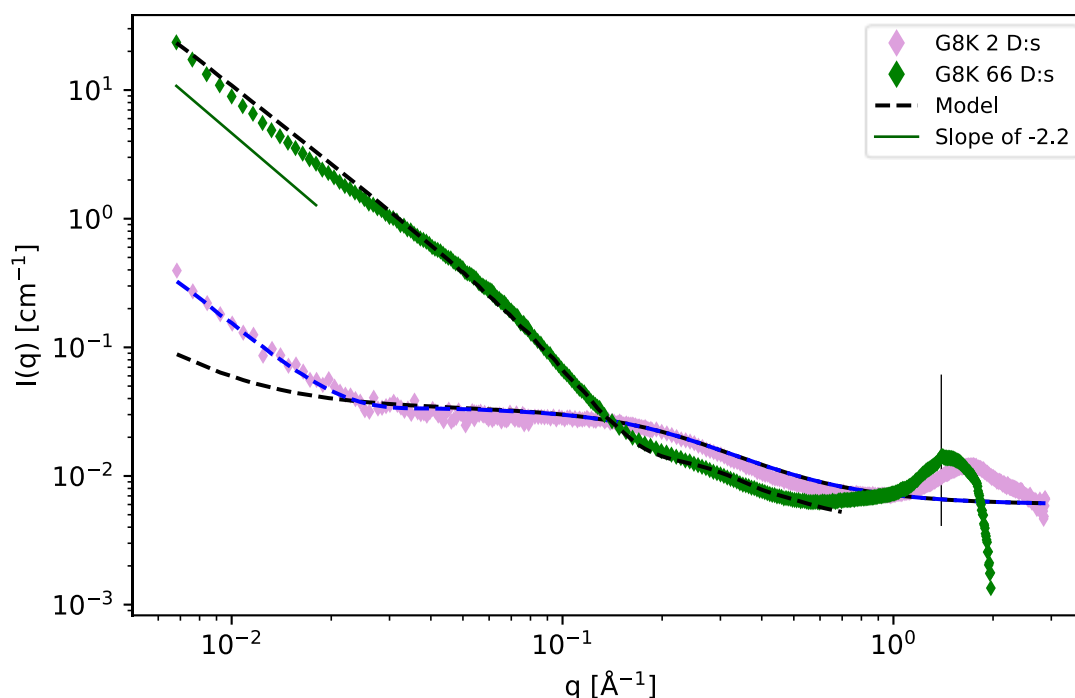


Figure 7. The scattering profile for a G8K 5 wt% sample measured at different waiting times, 2 and 66 days after preparation. The vertical line corresponds to a peak at  $q= 1.4 \text{ \AA}^{-1}$ , corresponding to  $4.5 \text{ \AA}$ . The presented models are a combination of discs and monomeric Gaussian polymer coils(www.sasview.com) model. The blue model for have a higher disc thickness compared to the black model. For the polymer coil model, the radius of gyration is set to 7 Å. Exact parameters for the model can be found in the appendix.

The main difference for the applied models in figure 7 for the different waiting times are the ratio between discs and monomeric polymer coils. The fraction of discs increases over time and the fraction of monomeric polymer coils decrease. While kinetics has not be the focus, this suggests that we se an increase in aggregation over time. The difference in stacking parameters for the different model, black and blue, is perplexing.

In figure 8 a cryo TEM image of G8K aggregates is shown. An initial observation confirms the presence of a two-dimensional shapes, showing consistency with data given by SAXS measurements. Furthermore, clusters of laminated beta sheet discs in different orientations can be observed as well as a couple of single discs. Moreover, the following image, 9, shows the same sample at a longer time from preparation. The distribution of the sheets is more uniform and not as clustered as in figure 8. Furthermore, in figure 11 A, a close-up image of a stack of G8K sheets is shown. A line scan, as shown in figure 11 B, shows the distance between layers within the discs approximates to 3 nm. This is about the length of a single stretched G8K peptide.

From the cryo images we derive the parameters previously set for the models in figure 7. The stacking of discs is derived from the shown clusters of discs.

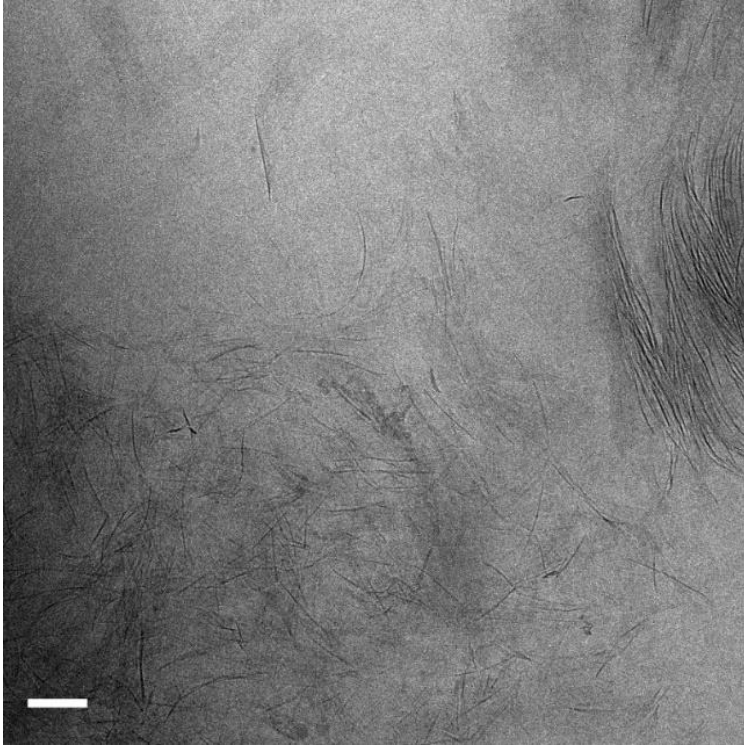


Figure 8 A cryo TEM image of G8K diluted from 5 wt% to 3 wt%. Discs in different orientations can be observed well as clusters of discs. The scale bar is 100 nm.

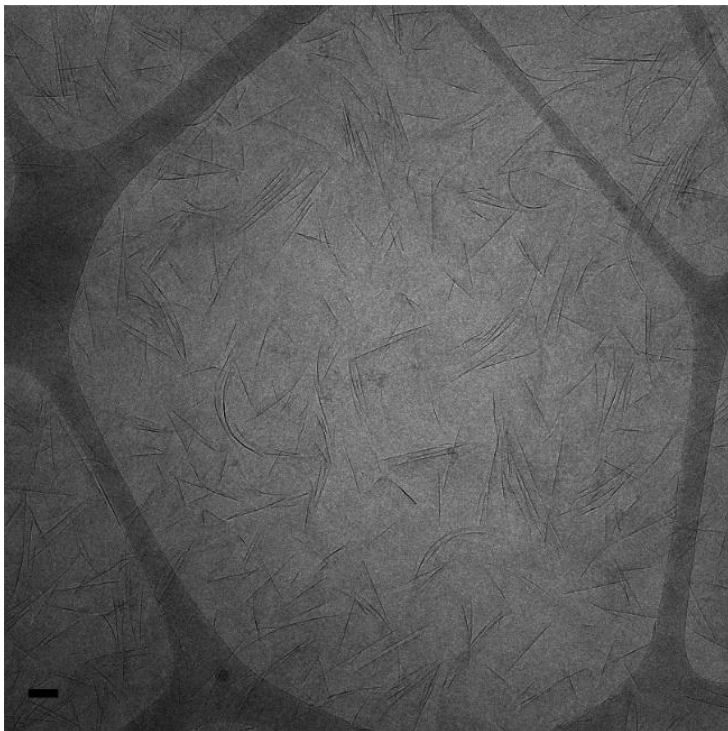
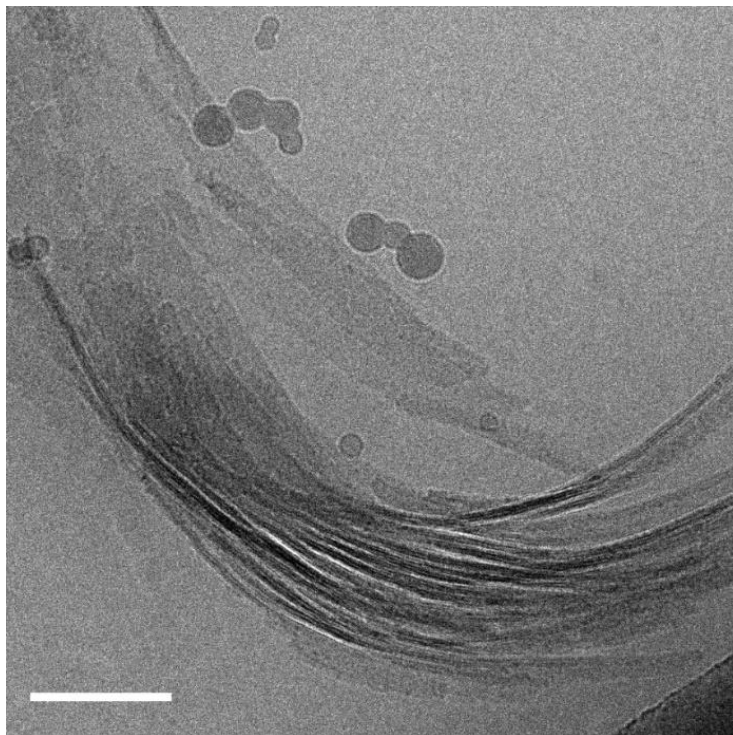


Figure 9. A cryo TEM image of G8K diluted down from 5 wt% to 1 wt% The sample is the same as in figure 9 but the image is taken approximately 50 days later. The scale bar (bottom left corner) is 100 nm.



**Figure 10** A cryo TEM image of G8K diluted from 5 wt% to 0.03 wt%. Stacks of sheets can be observed. The scale bar is 100 nm

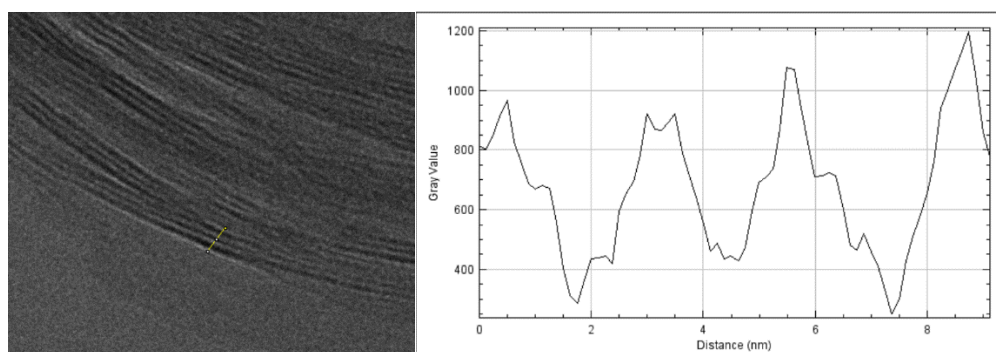


Figure 11 A(left) & B(right). Close-up of internal stacking within the different layers(left) The graph(right) shows the grey scale variation along the line seen in the left image. The y-axis in the graph, indicates the brightness of the analysed area. The three valleys in the graph, corresponds to the three darker lines highlighted by the yellow line(left). Distance corresponds to the length of a G8K peptide chain.

For further elucidation of the G8K aggregates CD measurements were made but the data proved unreliable to interpret, as shown in figure 12. This is due to that only lysine(K) in the G8K model peptide is chiral. Thus, CD measurements for G8K proved to be of no use for the characterization of G8K. Another approach was taken, and ATR FTIR measurements were made instead.

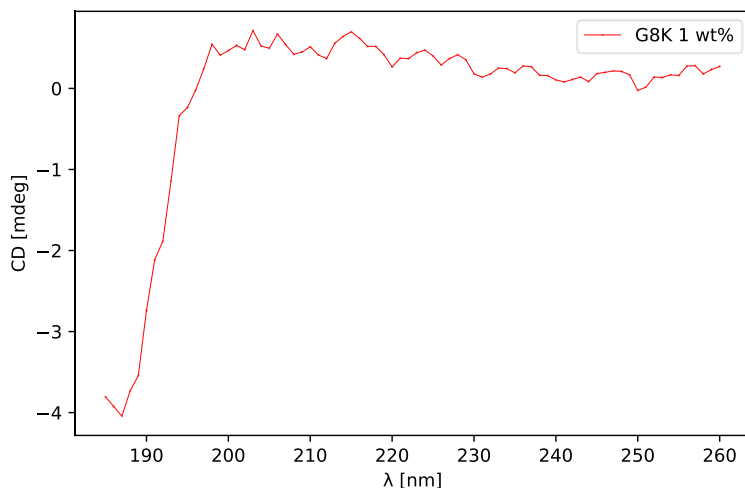


Figure 12. CD spectra of G8K. Shows some resemblance of random coil but is shifted to far to lower wavelengths.

In figure 13 a spectrum of G8K is shown. In this work we have focused on the amide I region,  $1600\text{-}1700\text{ cm}^{-1}$ , as this is the region from which protein secondary structures can usually be determined (Grdadolnik, 2003). There is also some water left that was not subtracted with the background, the leftover causes the intensity shifting areas at  $3500\text{ cm}^{-1}$  and just above  $2000\text{ cm}^{-1}$  (Barth, 2007).

An initial analysis would suggest that we have a parallel or anti-parallel beta sheet structure due to the peak at  $1630\text{ cm}^{-1}$  (Haris, 2013; Haris & Chapman, 1995). For an anti-parallel beta sheet there is also a supposed high frequency component at  $1685 \pm 10\text{ cm}^{-1}$ . This is however widely debated, discussed and reported (Cesare M Baronio et al., n.d.; Cesare Michele Baronio, 2020; Barth, 2007; Barth & Zscherp, 2002; Haris & Chapman, 1995; Jabs, 2013; Khurana & Fink, 2000; Krimm & Bandekar, 1986; Rabotyagova et al., 2010; Susi, And & Michael Byler, 1987; Valenti et al., 2011). However, through personal correspondence with A. Barth it was highly suggested that we can observe the high frequency component for several of our peptides. Further analysis is needed however, such as a second derivative analysis of the peaks in the amide I region.

The amide I region in this case have problematic contributions that needs to be considered. Since the water subtraction is unsatisfactory, it is possible that there is still a contribution in the amide I region from a scissoring vibration from the water molecule (Barth, 2007). Moreover, the peptide counterion, (TFA), is also contributing with an absorbance band at  $1673\text{ cm}^{-1}$  (Valenti et al., 2011). The wavenumber of  $3297\text{ cm}^{-1}$  in the amide A region should also be as its frequency correlates with the strength of the hydrogen bond (Barth, 2007). Hydrogen bonds will lower the frequency of stretching vibrations as it lowers the restoring force when the hydrogen bonds are in the vicinity of each other (Barth, 2000). A slight shift to the right of the amide I region there is the amide II peak at  $1535\text{ cm}^{-1}$ . As the amide II region is a combination of several minor contributions, secondary structure determination here is not be as straight forward. Just below  $1500\text{ cm}^{-1}$  the sidechain contribution can be observed. The TFA is also absorbing at  $1147\text{ cm}^{-1}$  and  $1200\text{ cm}^{-1}$  (Valenti et al., 2011).

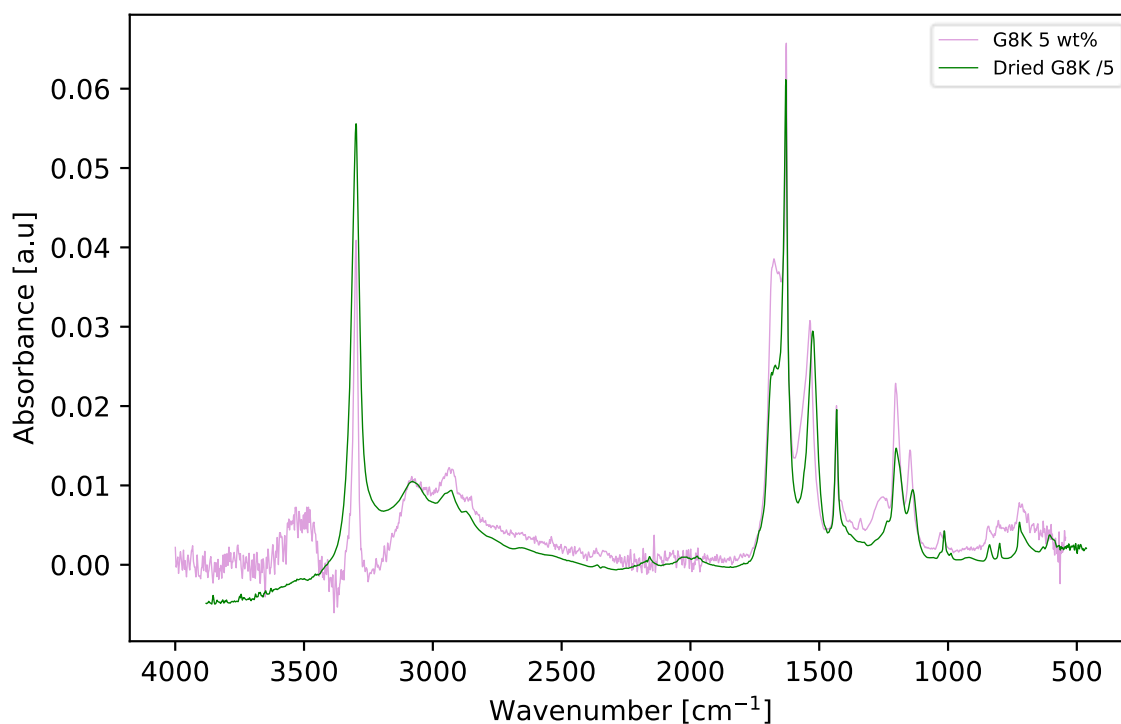


Figure 13 FTIR spectra of dried G8K and G8K (aq) 5 wt%. The intensity of the dried G8K have been divided by a factor of five.

When the sample is left to dry the model peptide ratio of the signal will increase and that of water will disappear as observed in figure 14, the intensity at 3500  $\text{cm}^{-1}$  and just above 2000  $\text{cm}^{-1}$  are significantly lower. The absorbance at the amide I region is furthermore a bit clearer. A slight shift in absorbance frequency can also be observed for the Amide II region. A consequence of drying the peptide could be changes to the parameter of the aggregates, as seen in figure 14 in the amide II region.

In figure 14 several things may be noted. In the amide I region we can observe a couple of interesting things. There is a change in absorbance frequency for the amide II region to a lower frequency, indicating a change in the chemical environment for the contributions for the amide II region. There is a small noticeable shift in absorbance frequency for the 1629  $\text{cm}^{-1}$  peak indicating that drying the peptide could induce minor changes within the aggregate. At the higher wavenumbers in the amide I region we now get a much clearer image of the its contributions. With water out of the picture two peaks can be observed, one peak at 1673  $\text{cm}^{-1}$  due to the contribution from the counterion, TFA. The other one is at 1686  $\text{cm}^{-1}$ , which is attributed to that of an anti-parallel beta sheet structure.

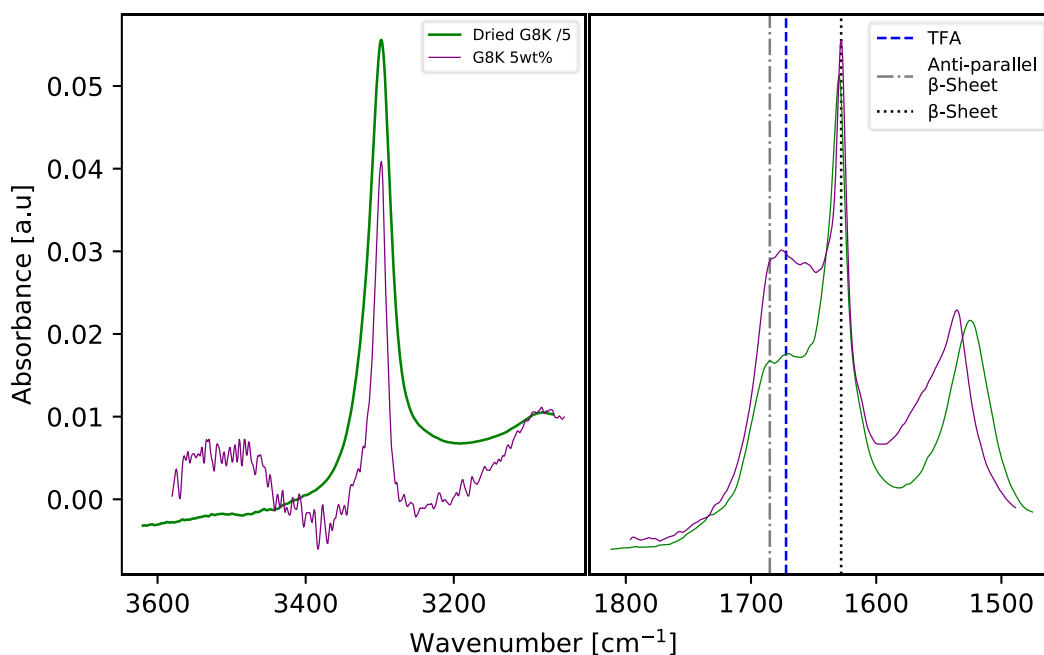


Figure 14. A close-up of the Amide A region(left) and Amide I region(right). Differences between dried and aqueous G8K is shown. The vertical lines indicate absorbance frequencies for TFA and beta-sheets in the amide I region. The intensity of the dried G8K have been divided by a factor five.

### 3.2 Comparing the self-assembly behaviour of the peptides A8K, KA8 and A4KA4

The self-assembly behaviour of A8K has previously been studied by (Cenker et al., 2014; Rüter, 2020). In this project we aim to characterize the impact on the self-assembly of moving the lysine within the primary structure of the model peptide. Thus, we have studied the KA8 with the lysine at the N terminus and A4KA4 with the lysine in the middle of the model peptide and we compare them with A8K.

As observed in figure 15, where we, again, present light scattering data as a function of peptide concentration, the CAC for KA8 is estimated to be just above 0.25 wt%. This is a slightly different value than for A8K of 0.14 W%(Cenker et al., 2014). More measurement should be made to corroborate the CAC deviation from A8K. An improvement for the measurement would be more data points, and more measurements. If one wants to derive conclusion from differences in CAC, the values for CAC should be more accurately determined. A larger difference in critical aggregation concentration is observed for A4KA4 in figure 15, compared to A8K. A4KA4 has an estimated critical aggregation concentration of just above 2 W%.

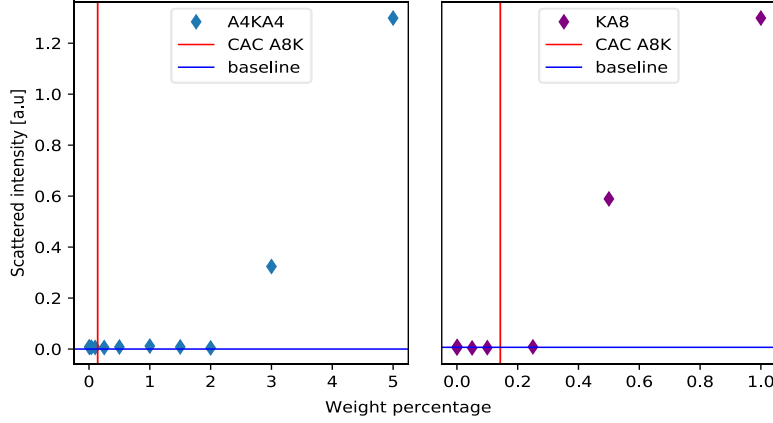


Figure 15. The scattered intensity as a function of weight percent for A4KA4(left) and KA8(right). A difference in scattered intensity from the baseline is derived from aggregates being formed. The baseline is the average value for the points of monomer scattering. CAC for A8K is shown for comparison.

The monomer solubility can be discussed in the terms of chemical potentials. There is a standard chemical potential,  $\mu$ , for the monomers in solution and in the aggregates, Eq 3 and 4. Where  $c$  is the concentration,  $k_B$  is the Boltzmann constant, and  $T$  is the temperature,  $\mu^\circ$  is the standard chemical potential, for monomers in solution(mon) and in aggregate(agg).

In solution we have another contribution, entropy of mixing, expressed as the second term in Eq 3. Aggregation occurs when the chemical potential for monomers in solution is higher than the chemical potential in the aggregates. Solving for when the aggregation occurs will lead to Eq 5 and is further visualized in figure 16. A possible derivation for the difference in solubility for A4KA4 and A8K can be explained by Eq 3-5 and figure 1.

We do not consider the alteration of the lysine group to have a noticeable impact on the chemical potential in solution for A4KA4, as shown in figure 17. However, imperfections in the aggregates caused by the inclusion of the bulky lysine group could have impact on the chemical potential for the monomers in their aggregated state, compared to A8K with the lysine at the end of the primary structure. As illustrated in figure 16, aggregation occurs when the two chemical potentials are equal, when the lines intersect.

$$\mu_{monomer} = \mu_{mon}^\circ + k_B T \ln(c) \quad (3)$$

$$\mu_{aggregate} = \mu_{agg}^\circ \quad (4)$$

$$Solubility, S = e^{((\mu_{agg}^\circ - \mu_{mon}^\circ)/k_B T)} \quad (5)$$

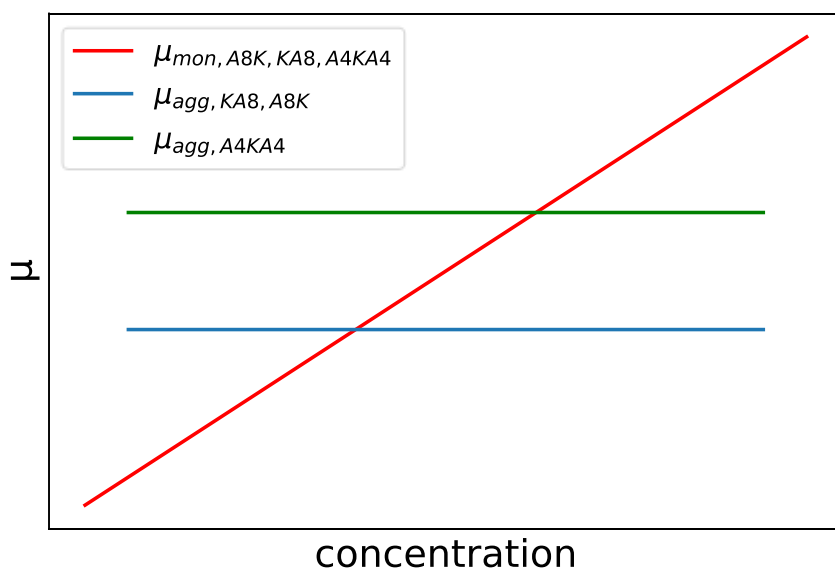


Figure 16. General presumption of the chemical potential for solutes in solution and in aggregated state. Based on Eq 1 and 2. The chemical potential for the monomers in solution is assumed to be the same.

The difference in solubility for A4KA4 is thus derived from a change in chemical potential for the monomer in the aggregates rather than the monomers in solution.

As an initial probe a CD measurement was made to get an estimate of secondary structure of the peptides. For KA8, shown in figure 17, there is a clear resemblance to that of A8K. Thus, the KA8 is assumed to aggregate into beta sheets (Cenker et al., 2014; Kelly et al., 2005).

CD measurements proved ineffective to determine the secondary structure of A4KA4, as there was excessive absorbance at concentrations below the CAC for A4KA4. We have no explanation for this now. There is, however, a slight resemblance to a random coil absorbance fingerprint at lower concentrations as seen in figure 18 (Kelly et al., 2005).

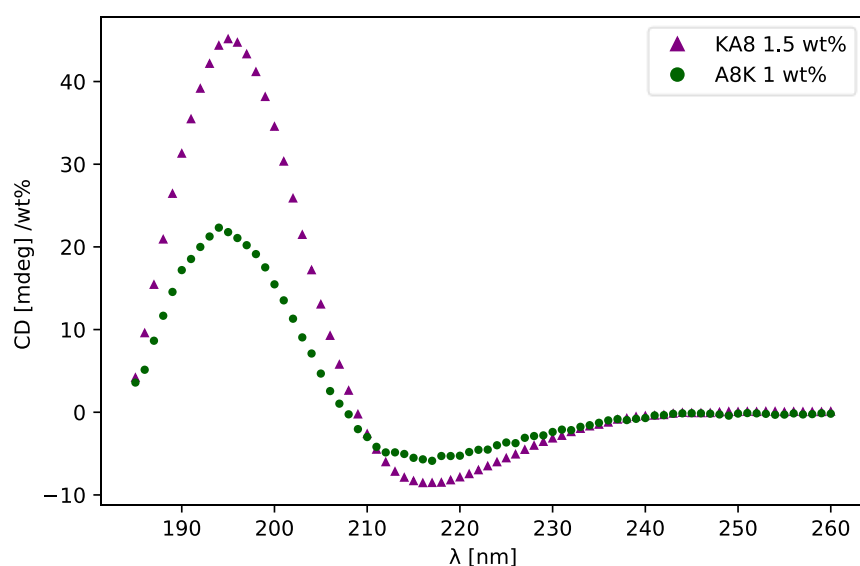


Figure 17 CD spectrum for KA8 and A8K. Normalized by weight percent.

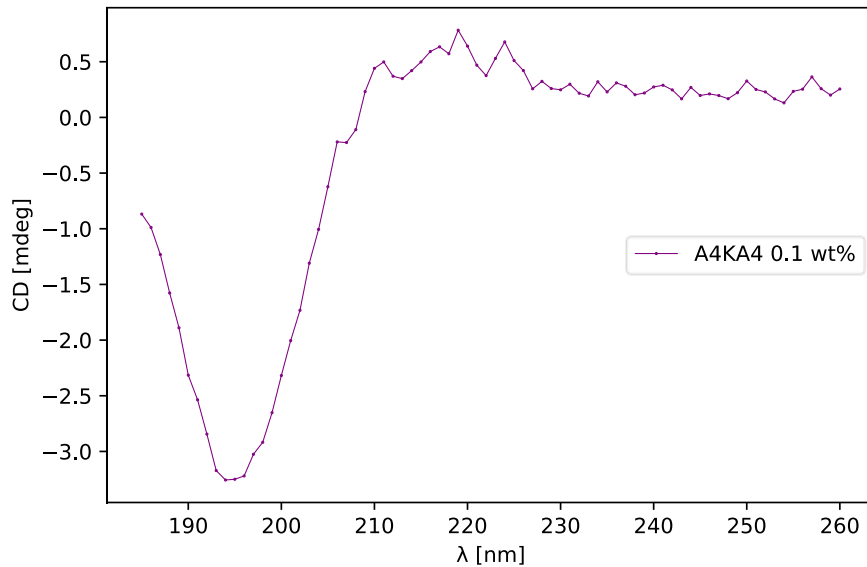


Figure 18. CD spectra for A4KA4 at 0.1 wt%.

Cryo TEM images, figure 19 A and B, shows several kinds of aggregated states of A4KA4. A network of fibrils can be observed. Along these fibrils are spherical clusters and unordered clumps of peptides. One hypothesis is that two different aggregates can be seen. The clusters along the fibrils could be derived from a fast aggregation step. While the longer fibrils take more time to crystallize as the bulky lysine sidechain creates a local disorder slowing down the crystallization progress. We suggest a two-step mechanism, first amorphous clusters are formed as an initial stage for a secondary nucleation. The second nucleation takes longer time as the lysine sidechain have to be accommodated within the crystalline structure(Lee & Terentjev, 2017).

Furthermore, twists of the fibril can be observed, as previously reported for A8K and A10K peptide aggregates (Rüter et al., 2019). This is interesting since the twist, which is present in A8K and A10K fibrils, is a common feature in aggregates of a chiral character(Rüter et al., 2019). The twisting of the fibrils stretches inter-peptide hydrogen bonds, creating a limit for aggregation sizes of the fibrils, due to high energy costs of stretched hydrogen bonds. The length of the A8K and A10K fibrils have previously been explained by the cost of the stretched hydrogen bonds caused by the twist of their fibres(Rüter et al., 2019). In the case of A4KA4, we have the occasional twists, but a length for the fibrils is beyond what we can observe. Furthermore, it would suggest that the cost of stretched hydrogen bonds is not as dominating for A4KA4, compared to A8K. The pitch of the twist is in the magnitude of a couple 100 nm as seen in figure 19 B, a great increase compared to earlier reported number of 12 and 16 nm(Rüter et al., 2019). Appreciated from figure 19 B, the width of the fibril is about 20 nm, the width of the fibrils is about a magnitude of 10 larger than for A8K.

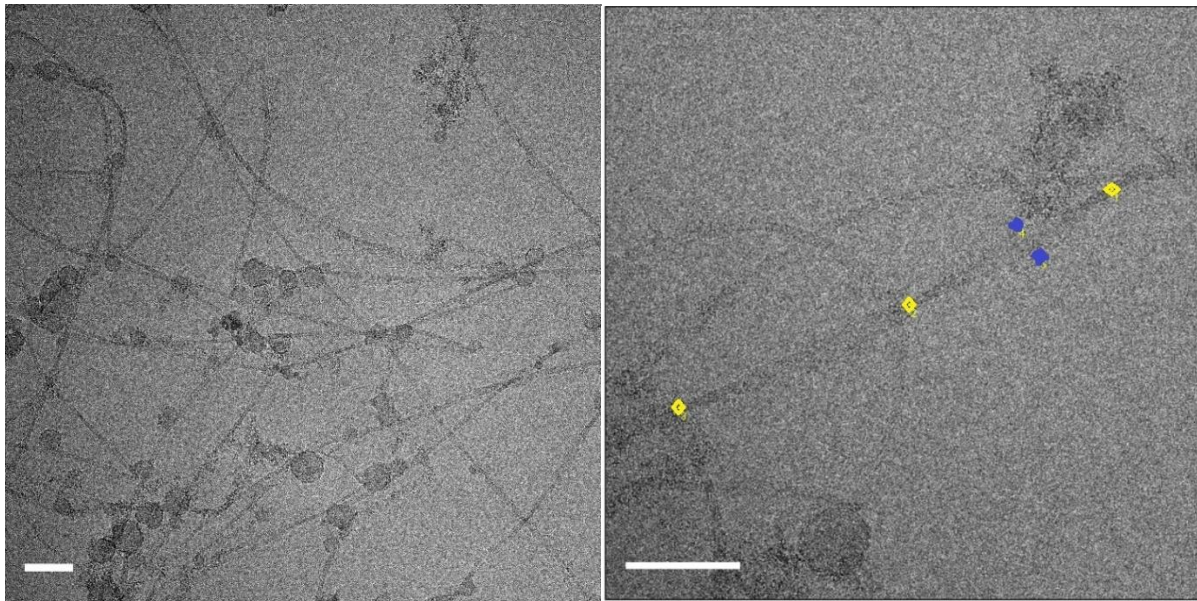


Figure 19 A(right) B(left). Cryo TEM images of A4KA4 with different magnifications. The samples were diluted down from 10 wt% to 0.1wt% The three yellow nodes along the axis of the fibre indicate twists. The two blue nodes indicate a width of about 20 nm. Scale bars are 100nm.

A 10 wt% A4KA4 solution was measured by SAXS to further determine its structure in its aggregated state. The scattering pattern can be observed along that of A8K in figure 20. At lower  $q$  values we can find the same wax pattern for A4KA4 as previously observed for A8K. We can note that the peaks in the WAXS region is broader for A4KA4 than for A8K. Indicating a less ordered systems in comparison with that of A8K. We assume that the bulky sidechain of lysine creates a local disorder for the packing peptides within the aggregates.

The three vertical lines in the same figure correspond to distances of  $5.4 \text{ \AA}$ ,  $4.5 \text{ \AA}$  and  $3.8 \text{ \AA}$ . The distance of  $3.8 \text{ \AA}$  have previously been reported as the distance of methyl groups and the oxygen in the peptide bond (Asakura et al., 2012). The other values, correspond to spacing of laminated beta sheets,  $5.4 \text{ \AA}$ , and beta strand spacing within beta sheets,  $4.5 \text{ \AA}$  (Kuczera et al., 2020). The initial slope of A4KA4,  $-1.75$ , indicates a difference compared to A8K with an initial slope of  $-1.14$ . An initial value of  $-1$  correlates to a structure estimated to be of a one-dimensional character (Schnablegger & Singh, 2011). A higher value for the initial slope could be derived from a structure factor caused by the network as seen in figure 19 A and B. Values closer to  $-2$  would indicate the presence of two-dimensional structures. The presence of several different aggregates in cryo TEM images might influence the value of the initial slope as there is a heterogeneity among the shapes of the observed aggregates in figure 19 A and B.

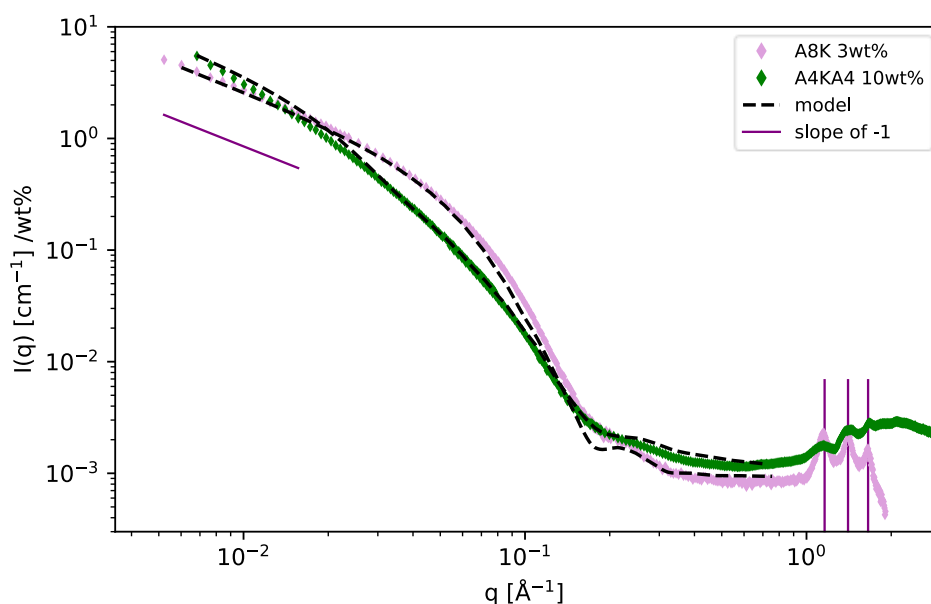


Figure 20. Scattering patterns for A8K and A4KA4. The A8K model is elliptical cylinders and for A4KA4 a combination of elliptical cylinders and monomeric gaussian polymer coils. The vertical lines mark  $q$ -values of  $1.65 \text{ \AA}^{-1}$ ,  $1.4 \text{ \AA}^{-1}$  and  $1.16 \text{ \AA}^{-1}$

The model used for A8K is an elliptical cylinder model with cross-section parameters used by (Rüter 2019, Cenker et al 2015), minor axis = 1.8 nm and an axis ratio of 2. The length of the aggregates is set far above the  $q$ -range for the measurement. A list of model parameters is presented in the Appendix. For A4KA4 the model achieves a better fit when changing the axis ratio. The model describes the data better using an axis ratio of 6, leading to  $a = 1.8 \text{ nm}$  and  $b = 10.8 \text{ nm}$ . The value of  $b$ , the major axis of the elliptical cylinder, agrees with the image analysis of cryo TEM images of A4KA4, as shown in figure 19 B, as a width of approximately 20 nm for the fibril is given by figure 19 B.

The scattering patterns for KA8 and A8K only differ slightly, the intensity at lower  $q$ -values and the shoulder at  $0.2 \text{ \AA}^{-1}$ . The characteristics of this shoulder correlates is strongly affected by chosen cross-section parameters of the elliptical cylinder. The difference in the model parameters for A8K and KA8, in figure 21, is a difference in cross-section parameters. As mentioned earlier, A8K aggregates have cross-section values of  $a = 1.8 \text{ nm}$  and  $b = 3.6 \text{ nm}$ . The model for KA8 fits better for values of  $a = 2.2 \text{ nm}$  and  $b = 4.4 \text{ nm}$  for the minor and major axis of the elliptical cylinder. Given the explanation made by (Rüter, 2020) for the structure of the fibrils, an increase in laminated beta sheets would only lead to a larger major axis for the elliptical cylinder. That does not explain the better fit for a value of 2.2 nm for the minor axis, we assume that this might be an artefact of using the models as an approximation for the systems we intend to describe.

The higher intensity at lower  $q$ -values is surprising given that the CAC of the peptides are not unsimilar. One explanation can be derived a difference in the mass per unit length, as it is proportional to the scattered intensity (Glatter, 2018). The difference in intensity approximately shares its ratio,  $\sim 1.5$ , with that of the area of the cross-sections for the different peptides given by the model parameters. However, it should be noted that the KA8 sample was measured first after 66 days and kinetics for KA8 aggregation have not been explored. Thus, conclusions from differences in intensity should be made carefully.

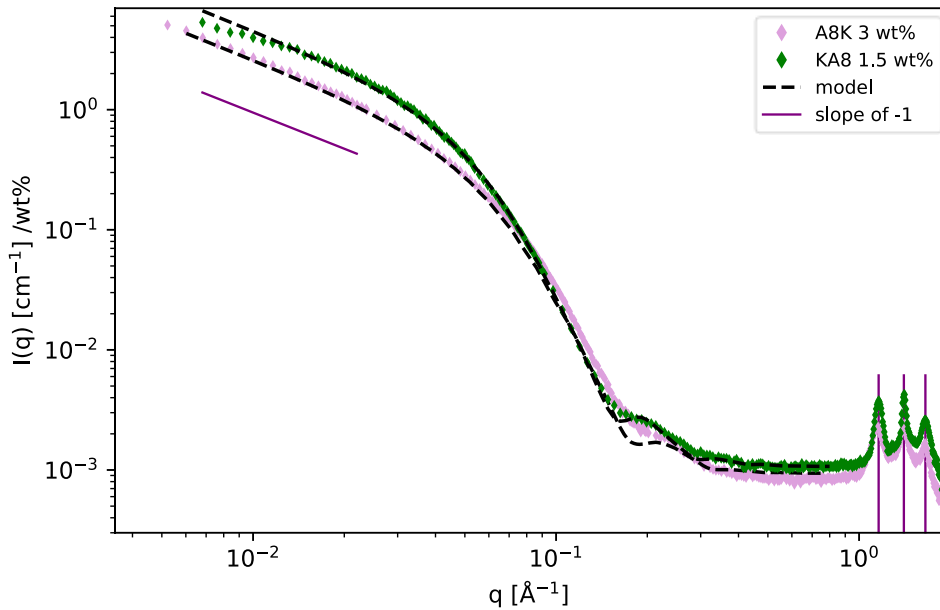


Figure 21. Scattering pattern for KA8 and A8K. The models correspond to scattering curves for elliptical cylinders. The vertical lines mark distances of 1.65, 1.4 and 1.16 Å<sup>-1</sup>

In figure 22 the FTIR absorbance spectrum of A4KA4 is presented. The frequency of the major absorbing peak in amide region A and II are consistent across both model peptides. This strongly suggests that we have the same type of secondary structure for our aggregated model peptides. Water has not been fully subtracted as water contributions are still observed at 3500 cm<sup>-1</sup>. Moreover, the amide I region for A4KA4 is not as clear as for A8K. Yet again water contributions might interfere with the spectra. In the amide II region, we can observe a split of the peak for A4KA4, we have no explanation for this.

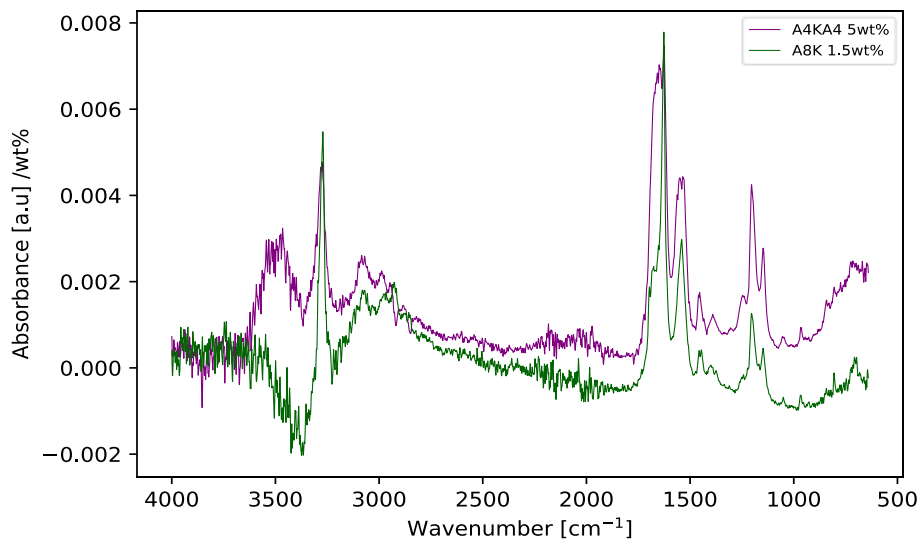


Figure 22. FTIR spectra of A8K and A4KA4

FTIR measurements of A8K and KA8 continue along the same results as for the analysis of the scattering patterns. In Amide regions I, II and A we can only see minor differences between A8K and KA8, as shown in figure 23. The higher intensities at the dominating peaks at the

amide I and A region for KA8 suggests that there is a difference between A8K and KA8 when they have aggregated. We expect that their intensities would be similar due to their close CAC.

In figures 23 and 24 we show a close-up of the amide regions A and I for A8K, KA8 and A4KA4. In figure 24, the samples were left to dry before measuring.

For the aqueous sample we can see that A8K and KA8 are similar. There is a slight shift for the amide II peak, and as noted before a difference in intensity between the two. For A4KA4 we can observe several things of interest. The peaks for amide A and I are split. A common denominator is the NH group for these regions. A possible hypothesis is that water might be present in a less ordered system that might include bulges in the beta sheet, interacting with the NH groups of A4KA4. There is still water present and the amide I region shows no clear preference for any secondary structure as there is no clear absorbance pattern correlating to a secondary structure.

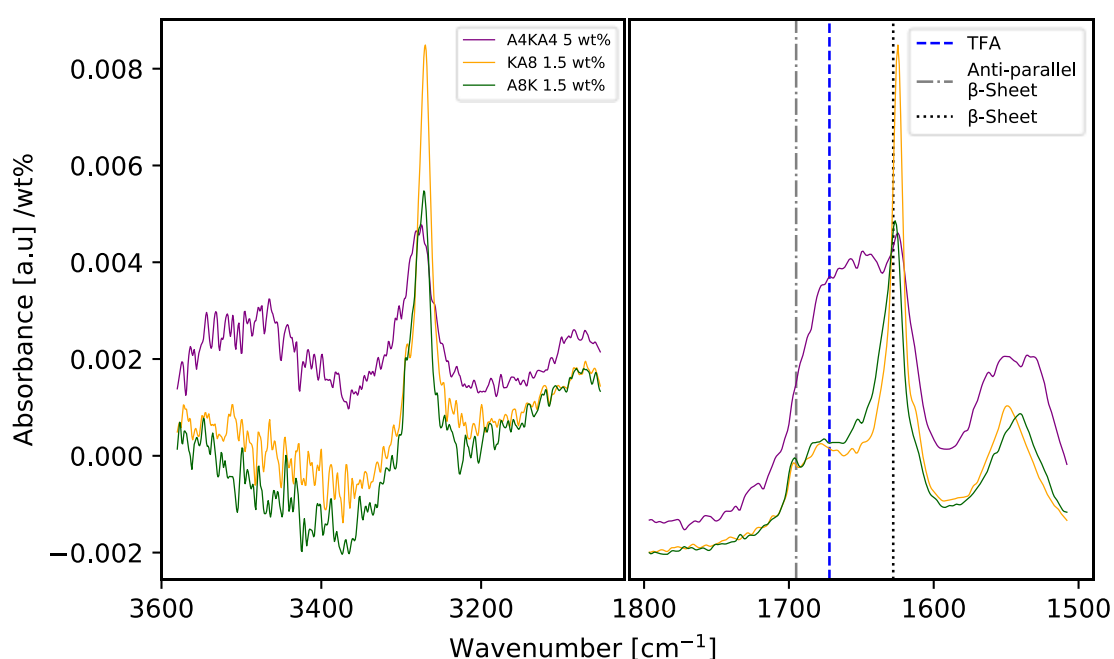


Figure 23 Amide region A(left) and I(right) for A8K, KA8 and A4KA4. The vertical lines correspond to absorbance frequencies expected for TFA and beta-sheets.

If the samples are left to dry and then measured, we get easily interpretable results as shown in figure 24. We should have in mind that we might induce artefacts by drying the samples, thus creating a deviation from otherwise observed behaviour. It is likely that the water subtraction for A4KA4 was insufficient, as the amide I regions is clearer from contributions and the absorbance at  $3500\text{ cm}^{-1}$  is gone in figure 24, as the sample have dried.

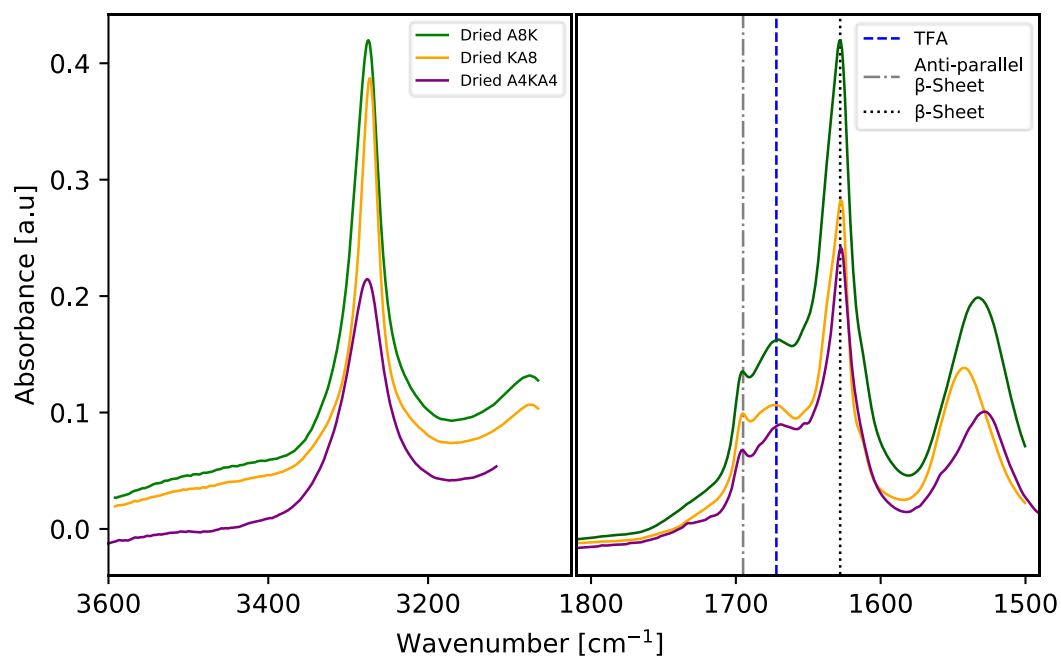
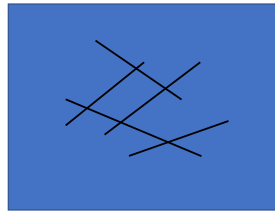


Figure 24. FTIR spectra of amide region A(left) and I(right) for dried samples of A8K, KA8 and A4KA4. The vertical lines correspond to absorbance frequencies expected for TFA and beta-sheets.

Furthermore, the spectra for A8K and KA8 become slightly clearer as we can see peaks corresponding to expected values of an anti-parallel beta sheet and TFA. Furthermore, the peaks align for the amide A peak, as opposed to the peaks when in solution as seen in figure 23. For the amide I region we can for the first time observe a distinct pattern aligning with values correlating to an anti-parallel structure (Barth & Zscherp, 2002). With peaks at  $1630\text{ cm}^{-1}$  and  $1695\text{ cm}^{-1}$  our conclusion is that the secondary structure is an anti-parallel beta sheet. The Amide II region is also interesting as all model peptides have a slight change in their absorbance frequency, hinting at some slight difference between the aggregates for the different model peptides. The contribution from TFA is present at  $1673\text{ cm}^{-1}$ .

We also note that at equal concentrations  $1.5\text{ wt}\%$ , A8K forms weak a gel but KA8 does not. KA8 instead appears as a viscous liquid, seemingly without any gel-like behaviour present. Presumably, the A8K aggregates are longer than in KA8, and therefore overlap at  $1.5\text{ wt}\%$  as shown in figure 25. Longer aggregates would give a different aspect ratio. The aspect ratio is the length of the fibril divided by its diameter. With longer fibrils A8K would have a higher aspect ratio. The aspect ratio determines the concentration where the system forms a gel (Rüter, 2020).



A8K 1.5 wt%



KA8 1.5 wt%

Figure 25 A8K (left) and KA8 (right). At 1.5 wt% A8K forms a gel while KA8 remains as a liquid. A8K is shown at the bottom its vial (upside-down). The difference in behaviour is derived from changes in aggregate length as illustrated.

### 3.3. Binary mixture peptides

#### 3.3.1 Binary mixture of A6K and A10K

It is known, that at one weight percentage A6K does not form aggregates and appears as monomers in solution. Furthermore, A6K has a CAC at about twelve weight percentage. The model peptides themselves have been characterized before by (Cenker et al., 2011; Rüter, 2020). The reason for these measurements was twofold. Do the mixed model peptides aggregate together, and will they adapt the structure of A6K or A10K?

If we observe the scattering pattern in figure 26 it becomes clear that the aggregate resembles that of A10K. Furthermore, the higher the fraction of A10K the more closely the scattering pattern resembles that of A10K, but at different intensities. It should be noted that the intensity at lower  $q$ -values do not decrease for the mixtures of equal amount or more of A6K, this could be because structure factor effects. Possibly indicating that the aggregates formed are longer than for aggregates where A10K is the dominating part. The decrease in intensity for the 1:3, A6K:A10K, solution is consistent with observed behaviour of A10K and is caused by electrostatic repulsive effects of the aggregates. These repulsive effects could be diminished by A6K monomers acting as “salt”, screening the electrostatic interactions for binary mixtures with a higher content of A6K, as is observed for the mixtures with more A6K.

However, as the differences in intensity are low, a quantitative analysis of coaggregation lacks support. An  $^1\text{H-NMR}$  experiment could be used to determine monomeric concentrations for the different solutions and thus support a quantitative analysis of coaggregation between A6K and A10K.

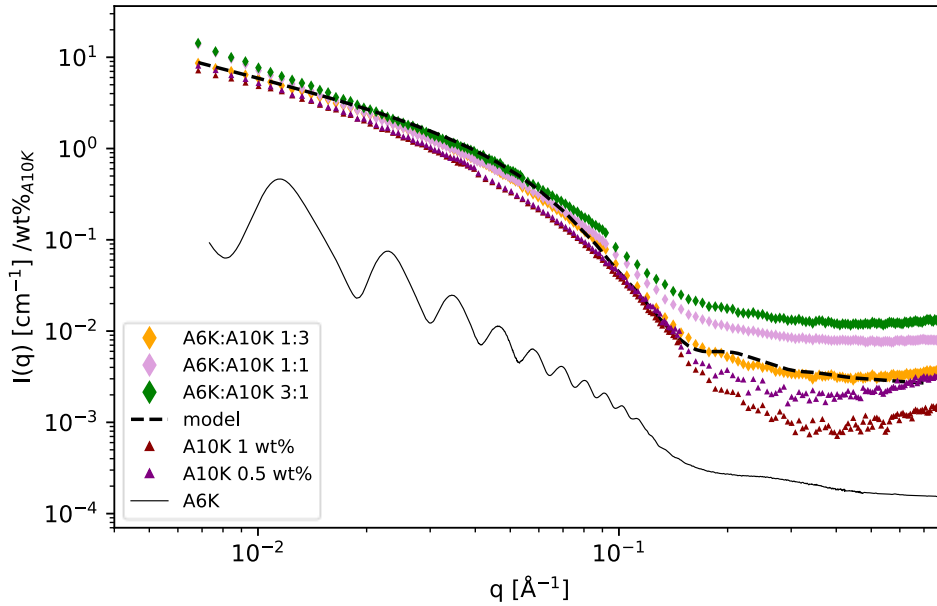


Figure 26. Scattering profiles of different ratios of A6K and A10K, adding up to one total weight percent of peptide. Scattering from the A6K and A10K model peptides are plotted along with the binary mixtures of them both. The model is a combination of elliptical cylinders and a monomeric Gaussian polymer coil. A6K scattering pattern shown for comparison.

### 3.3.2 Binary mixture of A8K and KA8

In figure 27 we can see the scattering pattern for the mixture of A8K and KA8. The characteristic bump at  $0.2 \text{ \AA}^{-1}$  is a little less distinct for the binary mixture. At lower  $q$ -values we can see a decrease in intensity, consistent with that of KA8. Furthermore, a slight negative deviation from the model. The difference in intensity at lower  $q$ -values are consistent with earlier data presented in figure 21, and are explained with the higher mass per length unit (Glatter, 2018), derived from the differences in cross-section areas for the different peptides.

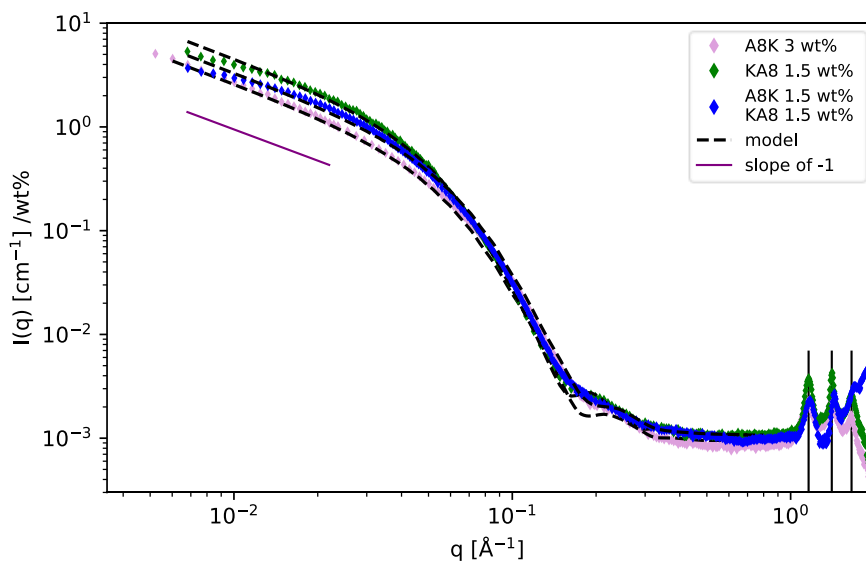


Figure 27. Scattering patterns for A8K, KA8 and the mixture of the two. The models are elliptical cylinders. The vertical lines mark distances of  $1.65$ ,  $1.4$  and  $1.16 \text{ \AA}^{-1}$

The mixture and the linear combination of the model peptides A8K and KA8 have no remarkable differences, as shown in figure 28. The hypothesis was that the spectrum of the binary mixture would deviate from that of the sum of the individual spectra from the different model peptides. However, no remarkable differences can be seen, making it near impossible to tell if they aggregate together or form separate aggregates that might interact with each other.

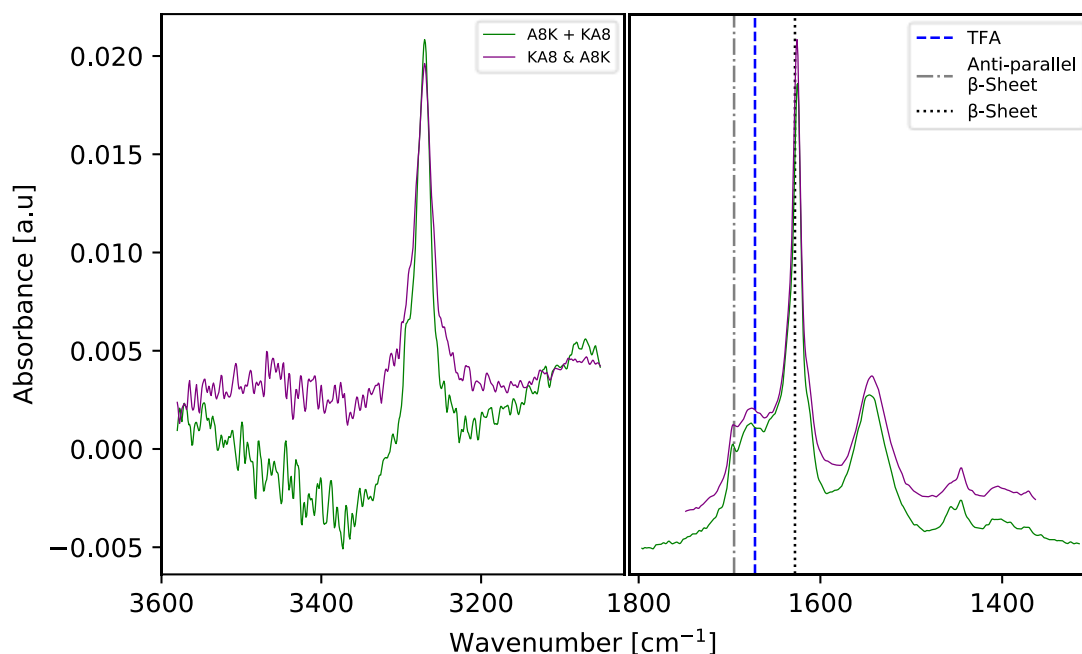


Figure 28. Close up of amide region I, II and A for the mixture and linear combination of A8K and KA8. Each peptide has a concentration of 1.5 wt%

We cannot conclude that they coaggregate with each other. There are some small differences in figure 28, in the amide I and II region. A possible conclusion is that the peptides interact with each other. But we cannot tell if we have aggregates interacting with each other or monomers in aggregates from both peptides. Deuteration and neutron scattering could give an answer, but such an experiment is beyond the financial capacity of this thesis.

### 3.3.3 Binary mixture of A8K and G8K

In figure 29 we present three different models. The dotted one is the same as in figure 7, a combination of thin discs and monomeric gaussian polymer coil. The dash-dotted model is for the combination of G8K and A8K. Thus, the model is a combination of elliptical cylinders and mono gauss coil as the scattering profile of the mixture resemblances that A8K rather than G8K. A larger contribution from monomers is also expected, as the shoulder around  $0.2 \text{ \AA}^{-1}$  is not as visible and G8K is below its CAC, further motivating the combination of models. Finally, the dashed model is elliptical cylinders as is the standard approach to model scattering for the A8K. Due to issues with the background subtraction at higher q-values the Bragg reflections are a hard to interpret. However, the Bragg reflections share similarities with A8K as the two initial peaks arise at the same q-values.

When modelling the mixture of the binary mixture, A8K/G8K, the model fits the data better when the cross-section parameters are slightly altered. A better fit for values axis minor = 2 nm and an axis ratio of 2 This is slightly longer than corresponding numbers for A8K, that has an

axis minor of 1.8 nm. One possible hypothesis is that achiral polyglycine parts of G8K might relieve the aggregate of twist induced stress. Thus, leading to slightly altered cross-section parameters for the combination of the model peptides.

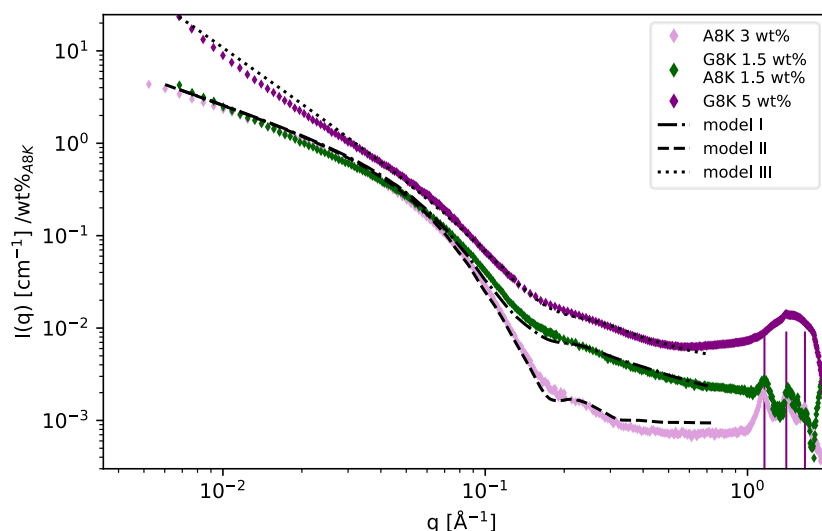


Figure 29. The scattering patterns for the A8K and G8K, and the binary mixture of the two. Model I, for the binary mixture, is a combination of elliptical cylinders and a monomeric gaussian polymer coil. Model II, for A8K, is an elliptical cylinder. Model III is a combination of thin discs and a monomeric Gaussian polymer coil.

One difference between G8K and A8K is the location of the peak in the amide A region, where G8K absorbs at a higher frequency than A8K, as shown in figure 30. This is most likely due to differences in hydrogen bonding strengths (Barth & Zscherp, 2002), hinting at slightly different spatial parameters within the aggregates of the two peptides. Furthermore, there is still some leftover water for G8K and the mixture of the peptides. In the amide A region, we can observe that the mixture absorbs at the same position as for A8K, although with a slightly higher intensity

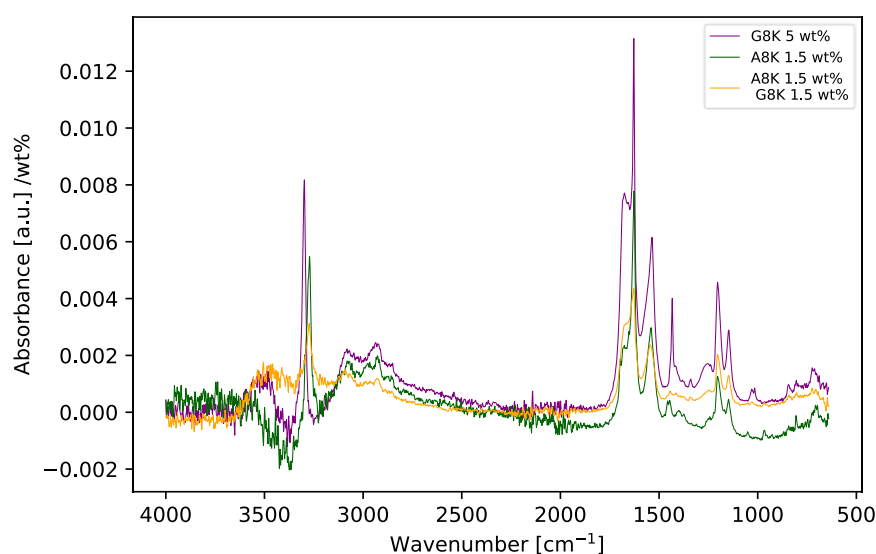


Figure 30. FTIR spectra of G8K and A8K, and the mixture of them both.

In figure 31 we can observe some minor differences at lower wavenumber attributed to different side chains of A8K and G8K (Barth, 2000). The amide II region has some slight shifts and peak patterns. The amide I region show similarities when it comes to the 1630  $\text{cm}^{-1}$  beta sheet peak. Its anti-parallel component is observable for A8K and is slightly hinted at for the mixture as a small bulge in the slope. For G8K the anti-parallel component appears at lower wavenumber, but still within range for what is acceptable for the anti-parallel component. The peak for G8K at 1433  $\text{cm}^{-1}$  is from a  $\text{CH}_2$  vibration (Taga et al., 1997). However, we cannot explain its absence in the binary mixture.

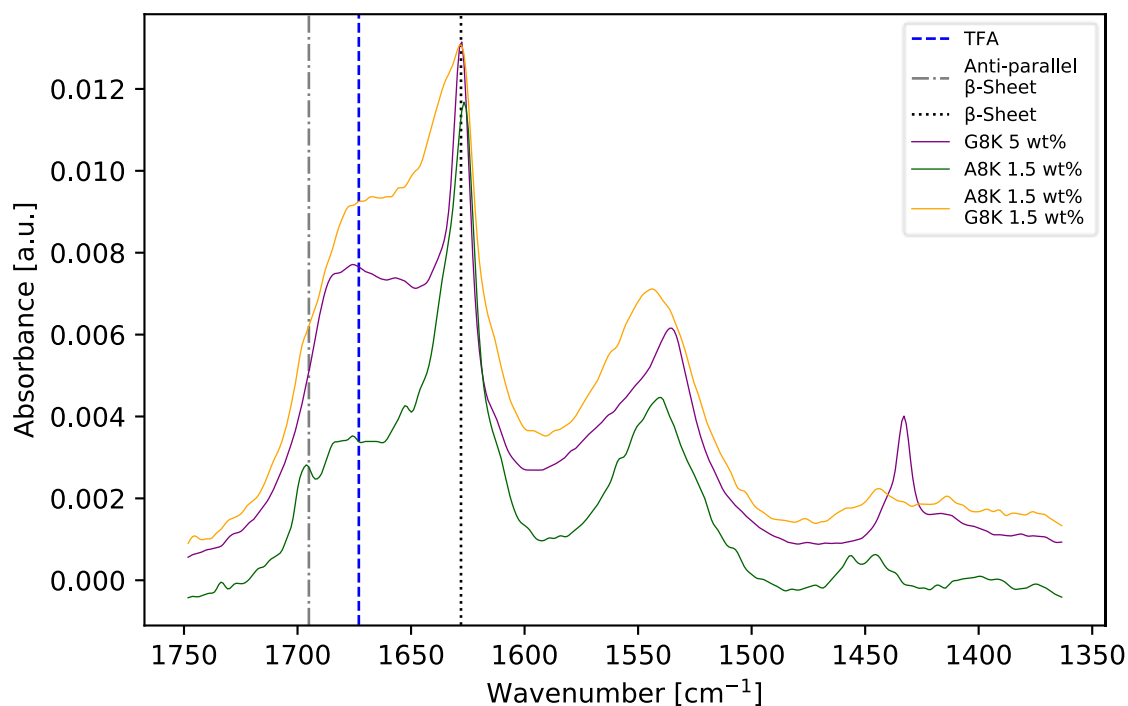


Figure 31 Close up of amide region I, II for A8K and G8K, and the binary mixture of G8K and A8K.

### 3.3.4 Binary mixture of KA8 and G8K

The models, in figure 32, for the different samples are the same as for the previous chapter, a combination of cylinder, elliptical cylinders and monomeric gaussian polymer coil. For G8K a combination of cylinders and monomeric gaussian polymer coil models were used. For KA8 elliptical cylinders were used and a combination of elliptical cylinder and monomeric gaussian polymer coil were used for the binary mixture. The combination of G8K and KA8 shows some remarkable traits. Same intensity at lower  $q$ -values and the same Bragg peaks. The same is not true for higher  $q$  values. As the monomeric contribution from G8K contributes to the intensity at these  $q$ -values.

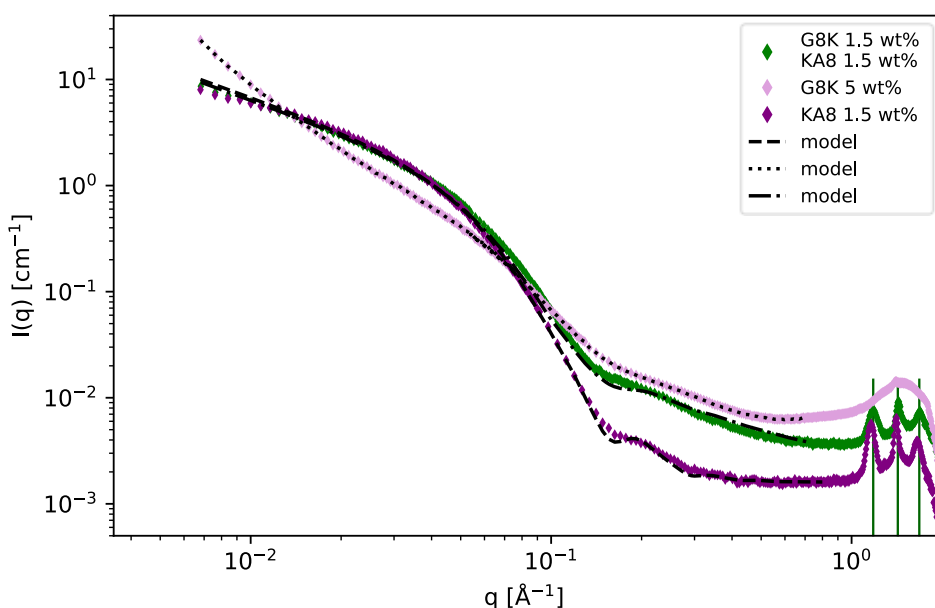


Figure 32 Scattering patterns for KA8 and G8K and their binary mixture. The models are the same as in figure 29. The vertical lines mark distances of  $1.65$ ,  $1.4$  and  $1.16 \text{ \AA}^{-1}$

If we look closely at the wide-angle scattering, figure 34, for G8K and KA8 we can observe a slight shift to higher  $q$ -values, matching slightly tighter packing parameters of the aggregate. This reflects including a peptide with a smaller molecular volume, G8K, in the packing matrix.

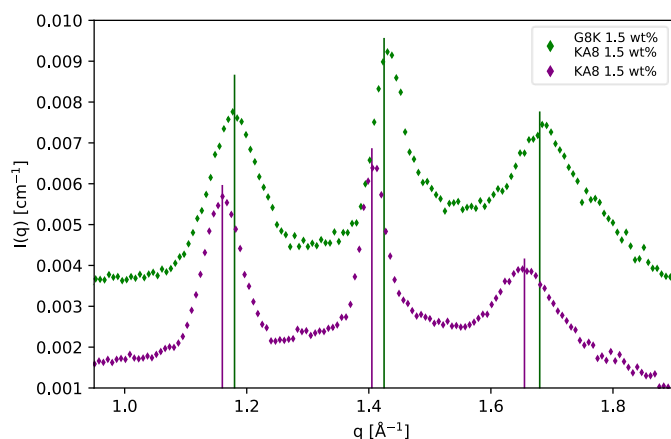


Figure 34. Wide angle scattering patterns for KA8 and G8K&KA8. A shift to higher  $q$ -values is shown.

As observed previously there is a difference in the amide A region. Compared to its alanine counterparts, G8K absorbs at a higher wavenumber, as shown in figure 35. Some leftover water from background subtraction is also visible for the binary mixture. When KA8 is involved it consistently correlates with a higher observable intensity, for FTIR and scattering experiments. Furthermore, we can observe the same pattern for the beta sheet peaks with one major peak around  $1630 \text{ cm}^{-1}$  and the anti-parallel component at  $1685 \pm 10 \text{ cm}^{-1}$  in figure 35. The increase in intensity from the singular KA8 peptide to the mixture of KA8 and G8K highly suggests coaggregation between the two peptides. An aggregate where the characteristics of KA8 is dominating. The amide I region has interference from water and the counter-ion, TFA, creating a diffuse area to decipher and analyse.

Hydrogen bonds increases the frequency of bending vibrations and lower the frequency of stretching vibrations. The amide A region have a major contribution from N-h stretching vibrations and the amide II region a contribution from N-H bending vibrations (Barth & Zscherp, 2002). This effect can be seen in the amide A and II region, as the frequency shift at the respective regions it reveals similarities when it comes to hydrogen bonds within the aggregates. The strengthens the hypothesis that KA8 and G8K aggregate together.

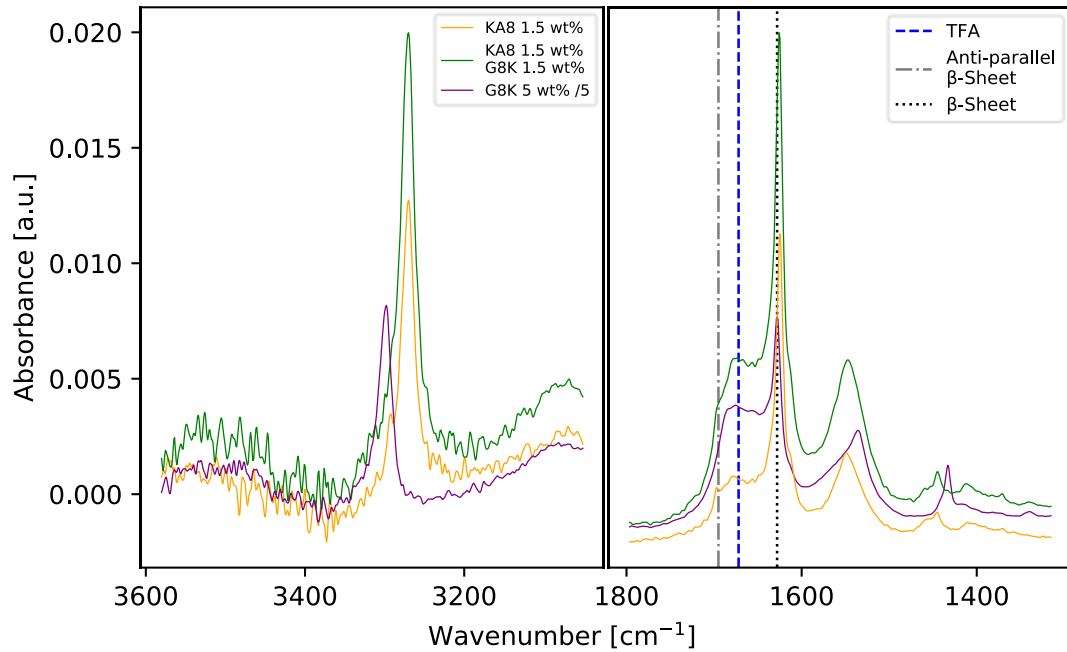


Figure 35 FTIR spectra of KA8 and G8K and the mixture of both peptides. G8K intensity have been divided by a factor five.

## 4. Conclusions

This chapter summarizes observed changes in secondary structures and self-assembly behaviour derived from changes of the primary structure of the model peptide. Furthermore, we address the binary mixture of peptides.

G8K expresses a major difference from the other model peptides, it is not as hydrophobic as its alanine counterparts. Furthermore, it lacks chirality for the polyglycine part of the peptide and thus an absence of intrinsic twists that is observed among chiral peptide molecules. This is derived from the fact that G8K forms two-dimensional aggregates as indicated by SAXS measurements and cryo TEM images.

For G8K we observe a difference in solubility from our light scattering measurements. A8K:s CAC is approximately 0.1 wt%(Cenker et al., 2014), while for G8K it is  $3\pm 5$  wt%. The difference in CAC from A8K is derived from the change in hydrophobicity. The peptide is not as prone to form beta-sheets as a model peptide with higher hydrophobicity at the same concentration

The peptide self-assembly have previously been described from a free energy perspective(Nyrkova et al., 2000; Rüter et al., 2019), being an interplay between hydrophobic interactions favouring aggregation and twists inducing stretched hydrogen bonds in the beta sheets, limiting the amount of possible laminated beta sheet. Hydrophobic effects prefer lamination of beta sheets in favour of the interaction with water. Furthermore, the deformation of the hydrogen bonds in G8K is not as pronounced as for its chiral counterparts, A8K and KA8, as the inherent twist of the model peptide is not present. The lack of chirality takes away the negative contribution from deformed hydrogen bonds. Thus, G8K forms large two-dimensional structures composed of beta sheets. It is highly suggested to form anti-parallel beta sheets as measured by ATR FTIR.

The A4KA4 peptide have a higher CAC, we hypothesise that this is due to a difference in chemical potential for the peptide in the aggregate. The bulky sidechain of lysine imposes defects and bulges in the assembled aggregate, increasing the chemical potential for the monomers in the aggregate. We can observe this in the WAXS scattering patterns were A4KA4 have broader peaks than A8K. The lack of short-range order might negate the effect of limiting twist factor found in A8K, as the packing is not as uniform the twist is not continuous throughout the aggregate.

At first glance KA8 shows great resemblance of A8K. Secondary structure for the peptides is the same, as confirmed by CD and FTIR. CAC is in the same order of magnitude. However, a closer inspection reveals some differentiating features. At the same concentration, 1.5 wt%, only A8K forms a macroscopic gel-like system. We derive this difference from different aspect ratios for the different peptides, assuming shorter aggregates for KA8(Rüter et al., 2020). In FTIR measurements we observe higher peaks in the amide I and A regions for KA8 at the same concentration as A8K. A difference in intensity is furthermore present at lower q values in scattering measurements as well. We hypothesise that the SAXS behaviour could be explained by KA8 having a different cross-sectional parameter than A8K, as determined by modelling SAXS data.

The binary mixture of A6K and A10K have proven problematic to determine if they aggregate together. As the SAXS measurements have not given data that is quantifiable enough to derive conclusions from differences in scattered intensity, which would indicate that they aggregate together. <sup>1</sup>H-NMR experiments would prove useful to determine monomer concentrations in solution for further studies.

Furthermore, the analysis of the mixture of KA8 and A8K have proven difficult. We do not have data that would support the hypothesis that they aggregate together. FTIR and SAXS data is to similar. However, small changes in FTIR spectra could justify a conclusion that they interact with each other, as aggregates or monomers in the same aggregate.

For the binary mixture of KA8, and G8K, we highly suggest that they coaggregate together. FTIR data for KA8 and G8K highly suggests that they coaggregate together as we can see an increase in intensity and shifts in frequency towards that of KA8. WAXS data further supports this as we can see a shift towards higher q-values, correlating with the inclusion of G8K with a smaller molecular volume in the crystalline packing. Finally, intensity in SAXS measurements further supports the hypothesis of coaggregation, as the mixture have a higher or equal intensity to that of KA8 by itself.

We make the same conclusion for A8K and G8K. The FTIR data highly suggests that they aggregate together due to the increased intensity. The fitting parameters for the model used to describe the scattering further supports that they coaggregate.

## 5. Outlook.

Further studies within the field of model peptide aqueous self-assembly could benefit from NMR-experiments to quantify monomer concentrations in binary solutions for example. In chapter 3.3.1 we conclude that we cannot quantify a difference in intensity for several binary mixtures. An <sup>1</sup>H-nmr experiment would be able to quantify the number of monomers left in solution.

FTIR experiments have been of great use in this work. Being able to interpret and derive information about whether the secondary structure of the aggregates is parallel or anti-parallel is a great step forward. It should be noted that only ATR-FTIR was used in this work and transmission FTIR could be of use as well for more accurate measurements. FTIR measurement have proven to be of great use.

## 6. Acknowledgements

First, I would like to thank my two supervisors I have had during this work, Ulf and Axel. Without their almost all-knowing knowledge, and support on the topic this work would not have been possible.

Secondly, I would like to thank the group that I've been a part of the last year. Marija, Viktoriia, Erika, Birte and Veronica, thank you for the wonderful time and all the interesting discussions.

Furthermore, I would like to thank Jon for helping me interpret my CD data.

I would like to thank Peter H. for our continuous discussion regarding on how to deal with mischievous Indian gods, it has been one of the reliable constants during my SAXS experiments.

Andreas for lending a hand in deciphering the issue of the anti-parallel component in my FTIR measurements.

I would also like to thank Cedric Dicko for the support with my FTIR measurements and the discussions regarding my data.

## 7. References

- Asakura, T., Okonogi, M., Horiguchi, K., Aoki, A., Saitô, H., Knight, D. P., & Williamson, M. P. (2012). Two Different Packing Arrangements of Antiparallel Polyalanine. *Angewandte Chemie*, 124(5), 1238–1241. <https://doi.org/10.1002/ange.201105356>
- Baronio, Cesare M, Li, H., Song, G., Thomas, H., Annecke, P., Martínez-carranza, M., Stenmark, P., & Barth, A. (n.d.). *The amide I spectrum of parallel  $\beta$ -sheet proteins* Cesare M. Baronio, Huimin Li, Guangyuan Song, Henry Thomas Pigott Annecke, Robert Gustafsson, Markel Martínez-Carranza, Pål Stenmark, Andreas Barth Department of Biochemistry and Biophysics, Stockholm Univ.
- Baronio, Cesare Michele. (2020). *Computational infrared Calculation of the amide I absorption of proteins*.
- Barth, A. (2000). The infrared absorption of amino acid side chains. *Progress in Biophysics and Molecular Biology*, 74(3–5), 141–173. [https://doi.org/10.1016/S0079-6107\(00\)00021-3](https://doi.org/10.1016/S0079-6107(00)00021-3)
- Barth, A. (2007). Infrared spectroscopy of proteins. *Biochimica et Biophysica Acta - Bioenergetics*, 1767(9), 1073–1101. <https://doi.org/10.1016/j.bbabi.2007.06.004>
- Barth, A., & Zscherp, C. (2002). What vibrations tell us about proteins. *Quarterly Reviews of Biophysics*, 35(4), 369–430. <https://doi.org/10.1017/S0033583502003815>
- Carroni, M., & Saibil, H. R. (2016). Cryo electron microscopy to determine the structure of macromolecular complexes. *Methods*, 95, 78–85. <https://doi.org/10.1016/j.ymeth.2015.11.023>
- Çenker, Ç. Ç., Bucak, S., & Olsson, U. (2011). Nanotubes and bilayers in a model peptide system. *Soft Matter*, 7(10), 4868–4875. <https://doi.org/10.1039/c0sm01186j>
- Çenker, Ç. Ç., Bucak, S., & Olsson, U. (2014). Aqueous self-assembly within the homologous peptide series AnK. *Langmuir*, 30(33), 10072–10079. <https://doi.org/10.1021/la5016324>
- Cukalevski, R., Yang, X., Meisl, G., Weininger, U., Bernfur, K., Frohm, B., Knowles, T. P. J., & Linse, S. (2015). The A $\beta$ 40 and A $\beta$ 42 peptides self-assemble into separate homomolecular fibrils in binary mixtures but cross-react during primary nucleation. *Chemical Science*, 6(7), 4215–4233. <https://doi.org/10.1039/c4sc02517b>
- De La Rica, R., & Matsui, H. (2010). Applications of peptide and protein-based materials in bionanotechnology. *Chemical Society Reviews*, 39(9), 3499–3509. <https://doi.org/10.1039/b917574c>
- Fosgerau, K., & Hoffmann, T. (2015). Peptide therapeutics: Current status and future directions. *Drug Discovery Today*, 20(1), 122–128. <https://doi.org/10.1016/j.drudis.2014.10.003>
- Glatter, O. (2018). *Scattering Methods and their Application in Colloid and Interface Science*. 97–109. <https://doi.org/10.1016/b978-0-12-813580-8.00005-5>
- Grdadolnik, J. (2003). Saturation effects in FTIR spectroscopy: Intensity of Amide I and Amide II bands in protein spectra. *Acta Chimica Slovenica*, 50(4), 777–788.
- Haris, P. I. (2013). Infrared Spectroscopy of Protein Structure. *Encyclopedia of Biophysics*, 1095–1106. [https://doi.org/10.1007/978-3-642-16712-6\\_135](https://doi.org/10.1007/978-3-642-16712-6_135)
- Haris, P. I., & Chapman, D. (1995). The conformational analysis of peptides using fourier transform IR spectroscopy. *Biopolymers*, 37(4), 251–263. <https://doi.org/10.1002/bip.360370404>
- Jabs, A. (2013). Determination of Secondary Structure in Proteins by Fourier Transform Infrared Spectroscopy (FTIR). *Jena Library of Biological Macromolecules*, 7. [http://www.imb-jena.de/ImgLibDoc/ftir/IMAGE\\_FTIR.html](http://www.imb-jena.de/ImgLibDoc/ftir/IMAGE_FTIR.html)
- Kelly, S. M., Jess, T. J., & Price, N. C. (2005). How to study proteins by circular dichroism. *Biochimica et Biophysica Acta - Proteins and Proteomics*, 1751(2), 119–139. <https://doi.org/10.1016/j.bbapap.2005.06.005>
- Khurana, R., & Fink, A. L. (2000). Do parallel  $\beta$ -helix proteins have a unique Fourier transform infrared spectrum? *Biophysical Journal*, 78(2), 994–1000. [https://doi.org/10.1016/S0006-3495\(00\)76657-4](https://doi.org/10.1016/S0006-3495(00)76657-4)

- Krimm, S., & Bandekar, J. (1986). Vibrational spectroscopy and conformation of peptides, polypeptides, and proteins. *Advances in Protein Chemistry*, 38(C), 181–364. [https://doi.org/10.1016/S0065-3233\(08\)60528-8](https://doi.org/10.1016/S0065-3233(08)60528-8)
- Kuczera, S., Rüter, A., Roger, K., & Olsson, U. (2020). Two dimensional oblique molecular packing within a model peptide ribbon aggregate. *ChemPhysChem*, 1–6. <https://doi.org/10.1002/cphc.201901126>
- Lee, C. T., & Terentjev, E. M. (2017). Mechanisms and rates of nucleation of amyloid fibrils. *Journal of Chemical Physics*, 147(10). <https://doi.org/10.1063/1.4995255>
- M. Dobson, C. (1999). Protein misfolding, evolution and disease. *Trends in Biochemical Sciences*, 24(September), 329–332.
- M. Doucet, et al. SasView Version 5.0.0 <http://doi.org/10.5281/zenodo.3011184>
- Nyrkova, I. A., Semenov, A. N., Aggeli, A., & Boden, N. (2000). Fibril stability in solutions of twisted  $\beta$ -sheet peptides: A new kind of micellization in chiral systems. *European Physical Journal B*, 17(3), 481–497. <https://doi.org/10.1007/s100510070127>
- Rabotyagova, O. S., Cebe, P., & Kaplan, D. L. (2010). Role of polyalanine domains in  $\beta$ -sheet formation in spider silk block copolymers. *Macromolecular Bioscience*, 10(1), 49–59. <https://doi.org/10.1002/mabi.200900203>
- Rüter, A. (2020). *On the colloidal and molecular aspects of peptide self-assembly*.
- Rüter, A., Kuczera, S., Gentile, L., & Olsson, U. (2020). Arrested dynamics in a model peptide hydrogel system. *Soft Matter*, 16(11), 2642–2651. <https://doi.org/10.1039/c9sm02244a>
- Rüter, A., Kuczera, S., Pochan, D. J., & Olsson, U. (2019). Twisted Ribbon Aggregates in a Model Peptide System. *Langmuir*, 35(17), 5802–5808. <https://doi.org/10.1021/acs.langmuir.8b03886>
- Schnablegger, H., & Singh, Y. (2011). *The SAXS guide, getting acquainted with the principles*. <https://austria-forum.org/web-books/en/saxs00en2013iicm/000072>
- Susi' And, H., & Michael Byler, D. (1987). Fourier Transform Infrared Study of Proteins with Parallel @-Chains. *Archives of Biochemistry and Biophysics*, 258(2), 465–469. <https://pdf.sciencedirectassets.com/272380/1-s2.0-S0003986100X04717/1-s2.0-0003986187903675/main.pdf?X-Amz-Security-Token=AgoJb3JpZ2luX2VjEhYACXVzLWVhc3QtMSJGMEQCIH9JmpMWnAVxyIp2o8O9bL3gLi%2Bbt1spI9CgIWvY6RGBAiB53HLEkgSLIBjVWwCQIu4HchGzYvXbertiZTjuzH4qHSr>
- Taga, K., Sowa, M. G., Wang, J., Etori, H., Yoshida, T., Okabayashi, H., & Mantsch, H. H. (1997). FT-IR spectra of glycine oligomers. *Vibrational Spectroscopy*. [https://doi.org/10.1016/S0924-2031\(96\)00061-6](https://doi.org/10.1016/S0924-2031(96)00061-6)
- Valenti, L. E., Paci, M. B., De Pauli, C. P., & Giacomelli, C. E. (2011). Infrared study of trifluoroacetic acid unpurified synthetic peptides in aqueous solution: Trifluoroacetic acid removal and band assignment. *Analytical Biochemistry*, 410(1), 118–123. <https://doi.org/10.1016/j.ab.2010.11.006>
- Zhang, S. (2003). Fabrication of novel biomaterials through molecular self-assembly. *Nature Biotechnology*, 21(10), 1171–1178. <https://doi.org/10.1038/nbt874>
- Zhao, X., Pan, F., & Lu, J. R. (2008). Recent development of peptide self-assembly. *Progress in Natural Science*, 18(6), 653–660. <https://doi.org/10.1016/j.pnsc.2008.01.012>
- Asakura, T., Okonogi, M., Horiguchi, K., Aoki, A., Saitô, H., Knight, D. P., & Williamson, M. P. (2012). Two Different Packing Arrangements of Antiparallel Polyalanine. *Angewandte Chemie*, 124(5), 1238–1241. <https://doi.org/10.1002/ange.201105356>
- Baronio, Cesare M, Li, H., Song, G., Thomas, H., Annecke, P., Martínez-carranza, M., Stenmark, P., & Barth, A. (n.d.). *The amide I spectrum of parallel  $\beta$ -sheet proteins Cesare M. Baronio, Huimin Li, Guangyuan Song, Henry Thomas Pigott Annecke, Robert Gustafsson, Markel Martínez-Carranza, Pål Stenmark, Andreas Barth Department of Biochemistry and Biophysics, Stockholm Univ.*

- Baronio, Cesare Michele. (2020). *Computational infrared Calculation of the amide I absorption of proteins*.
- Barth, A. (2000). The infrared absorption of amino acid side chains. *Progress in Biophysics and Molecular Biology*, 74(3–5), 141–173. [https://doi.org/10.1016/S0079-6107\(00\)00021-3](https://doi.org/10.1016/S0079-6107(00)00021-3)

## 8. Appendix

Model parameters.

Data loaded from: G8K\_190929.txt

Model | Fit Options | Resolution | Polydispersity | Magnetism

Model

Category: Plugin Models | Model name: G8K\_cylinder\_mono | Structure factor: None

Parameter	Value	M
<input type="checkbox"/> scale	1.0	0.
<input type="checkbox"/> background	0.006	-c
<b>G8K_cylinder_mono_gauss_coil</b>		
<input checked="" type="checkbox"/> A_scale	0.00001	-c
<input type="checkbox"/> A_sld	13.1	-c
<input type="checkbox"/> A_sld_solvent	9.4	-c
<input checked="" type="checkbox"/> A_radius	1500	0.
<input checked="" type="checkbox"/> A_length	30	0.
<input type="checkbox"/> B_scale	1.0	-c
<input type="checkbox"/> B_i_zero	0.028	0.
<input checked="" type="checkbox"/> B_rg	7	0.

Options:  Polydispersity,  Magnetism

Fitting details: Min range: 0.0068312 Å<sup>-1</sup>, Max range: 2.8804 Å<sup>-1</sup>, Smearing: None

Fitting error:  $\chi^2$  0.00036653

Show Plot | Fit | Help

Model parameters for G8K used in figure 7. Combination of the cylinder and monomeric Gaussian polymer coil.

Data loaded from: G8K\_190929.txt

Model | Fit Options | Resolution | Polydispersity | Magnetism

Model

Category: Plugin Models | Model name: G8K\_cylinder\_mono | Structure factor: None

Parameter	Value	M
<input type="checkbox"/> scale	1.0	0.
<input type="checkbox"/> background	0.006	-c
<b>G8K_cylinder_mono_gauss_coil</b>		
<input type="checkbox"/> A_scale	0.00001	-c
<input type="checkbox"/> A_sld	13.1	-c
<input type="checkbox"/> A_sld_solvent	9.4	-c
<input checked="" type="checkbox"/> A_radius	1500	0.
<input checked="" type="checkbox"/> A_length	180	0.
<input type="checkbox"/> B_scale	1.0	-c
<input type="checkbox"/> B_i_zero	0.028	0.
<input checked="" type="checkbox"/> B_rg	7	0.

Options:  Polydispersity,  Magnetism

Fitting details: Min range: 0.0068312 Å<sup>-1</sup>, Max range: 2.8804 Å<sup>-1</sup>, Smearing: None

Fitting error:  $\chi^2$  1.7071e-05

Show Plot | Fit | Help

Model parameters for G8K used in figure 7. Combination of the cylinder and monomeric Gaussian polymer coil. Difference in “A\_length” as an estimation of stacking discs.

Data loaded from: G8K\_191127.txt

Model | Fit Options | Resolution | Polydispersity | Magnetism

Model

Category: Plugin Models | Model name: G8K\_cylinder\_mono | Structure factor: None

Parameter	Value	Min
<input type="checkbox"/> scale	1.0	0.0
<input type="checkbox"/> background	0.004	-∞
<b>G8K_cylinder_mono_gauss_coil</b>		
<input type="checkbox"/> A_scale	0.0038	-∞
<input type="checkbox"/> A_sld	13.1	-∞
<input type="checkbox"/> A_sld_solvent	9.4	-∞
<input checked="" type="checkbox"/> A_radius	1000	0.0
<input checked="" type="checkbox"/> A_length	32	0.0
<input type="checkbox"/> B_scale	1.0	-∞
<input type="checkbox"/> B_i_zero	0.0165	0.0
<input checked="" type="checkbox"/> B_rg	7	0.0

Options:  Polydispersity,  Magnetism

Fitting details: Min range: 0.0068064 Å<sup>-1</sup>, Max range: 2.8735 Å<sup>-1</sup>, Smearing: None

Fitting error:  $\chi^2$  0.035958

Show Plot | Fit | Help

Model parameters for G8K(66 D:s). used in figure 7, 29 and 32.

Data loaded from: A4KA4.txt

Model | Fit Options | Resolution | Polydispersity | Magnetism

Model

Category: Plugin Models | Model name: A4KA4 | Structure factor: None

Parameter	Value	Min
<input type="checkbox"/> backgro...	0.0032	-∞
<b>A4KA4</b>		
<input type="checkbox"/> A_scale	0.004	-∞
<input checked="" type="checkbox"/> A_radius...	18	0.0
<input checked="" type="checkbox"/> A_axis_ra...	6	1.0
<input checked="" type="checkbox"/> A_length	10000	1.0
<input type="checkbox"/> A_sld	13.4	-∞
<input type="checkbox"/> A_sld_sol...	9.4	-∞
<input type="checkbox"/> B_scale	1.0	-∞
<input checked="" type="checkbox"/> B_i_zero	0.0036	0.0
<input checked="" type="checkbox"/> B_rg	5.5	0.0

Options:  Polydispersity,  Magnetism

Fitting details: Min range: 0.0068312 Å<sup>-1</sup>, Max range: 2.8804 Å<sup>-1</sup>, Smearing: None

Fitting error:  $\chi^2$  0.010412

Model parameters for A4KA4. Model is a combination of elliptical cylinders and monomeric Gaussian polymer coils. Used in figure 20.

Data loaded from: KA8.txt

Model | Fit Options | Resolution | Polydispersity | Magnetism

Model

Category: Cylinder | Model name: elliptical\_cylinder | Structure factor: None

Parameter	Value	Min	Max
<input type="checkbox"/> scale	0.0045	0.0	$\infty$
<input type="checkbox"/> backgro...	0.0017	$-\infty$	$\infty$
<b>elliptical_c...</b>			
<input checked="" type="checkbox"/> radius_m...	22	0.0	$\infty$
<input checked="" type="checkbox"/> axis_ratio	2	1.0	$\infty$
<input checked="" type="checkbox"/> length	10000	1.0	$\infty$
<input type="checkbox"/> sld	13.4	$-\infty$	$\infty$
<input type="checkbox"/> sld_solvent	9.4	$-\infty$	$\infty$

Options:  Polydispersity,  Magnetism

Fitting details: Min range: 0.0068064  $\text{\AA}^{-1}$ , Max range: 2.8735  $\text{\AA}^{-1}$ , Smearing: None

Fitting error:  $\chi^2$  0.021454

Model parameters for KA8. Used in figure 21, 27 and 32.

Data loaded from: A610K\_2575.txt

Model | Fit Options | Resolution | Polydispersity | Magnetism

Model

Category: Plugin Models | Model name: A4KA4 | Structure factor: None

Parameter	Value	Min
<input type="checkbox"/> scale	1.0	0.0
<input checked="" type="checkbox"/> background	0.0018	$-\infty$
<b>A4KA4</b>		
<input type="checkbox"/> A_scale	0.003	$-\infty$
<input checked="" type="checkbox"/> A_radius_minor	22	0.0
<input checked="" type="checkbox"/> A_axis_ratio	2	1.0
<input checked="" type="checkbox"/> A_length	10000	1.0
<input type="checkbox"/> A_sld	13.4	$-\infty$
<input type="checkbox"/> A_sld_solvent	9.4	$-\infty$
<input type="checkbox"/> B_scale	1.0	$-\infty$
<input type="checkbox"/> B_i_zero	0.0017	0.0
<input checked="" type="checkbox"/> B_rg	5.5	0.0

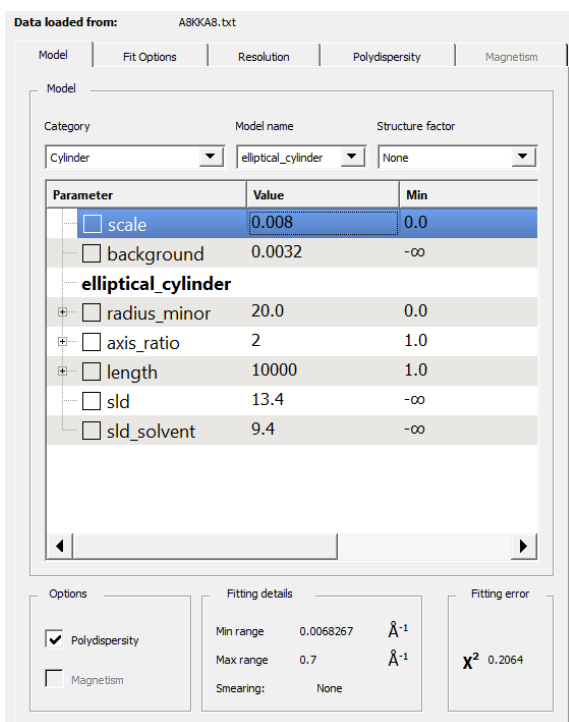
Options:  Polydispersity,  Magnetism

Fitting details: Min range: 0.006826  $\text{\AA}^{-1}$ , Max rang: 0.7  $\text{\AA}^{-1}$ , Smearing: None

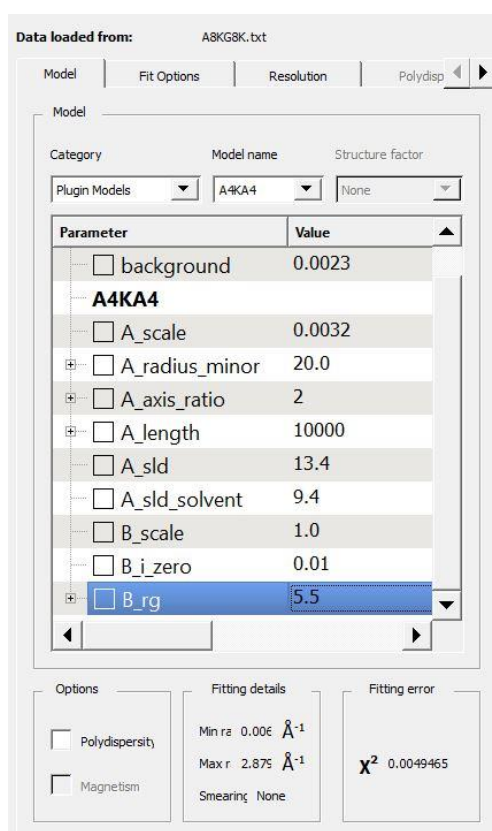
Fitting error:  $\chi^2$  0.0099629

Show Plot | Fit | Help

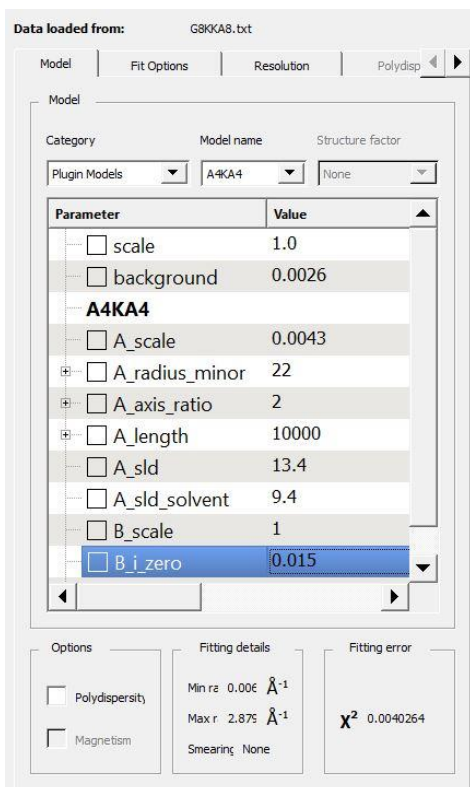
Model for A6K:A10K 1:3. Combination of a cylinder and monomeric Gaussian polymer coil. Used in figure 26



Model for the binary mixture of A8K and KA8. A PD ratio of 0.1 was set for the polydispersity of radius minor. Used in figure 27.



Model parameters for the binary mixture of A8K and G8K. The model is a combination of cylinders and monomeric Gaussian polymer coil. Used in figure 29.



Model parameter for the binary mixture of KA8 and G8K. The model is a combination of cylinders and monomeric Gaussian polymer coils. Used in figure 32.